Formability of Rolled and Extruded Magnesium Sheet

MICROSTRUCTURAL EFFECTS ON THE FORMABILITY OF ROLLED AND EXTRUDED MAGNESIUM SHEET

By
KENDAL S. DUNNETT, B.Eng.

A Thesis

Submitted to the School of Graduate Studies

in Partial Fulfilment of the Requirements

for the Degree

Master of Applied Science

McMaster University

MASTER OF APPLIED SCIENCE (2009) McMaster University
(Department of Materials Science and Engineering) Hamilton, Ontario

TITLE: Microstructural Effects on the Formability of Rolled and Extruded Magnesium Sheet

AUTHOR: Kendal S. Dunnett, B.Eng.

SUPERVISOR: Dr. David S. Wilkinson

NUMBER OF PAGES: x, 86

Abstract

The automotive industry has become a major user of magnesium components. However, use of magnesium sheet products is quite limited, due to difficulties in producing cost effective components. Any sheet currently produced is formed at elevated temperatures, making magnesium parts relatively expensive. Knowledge of the microstructural effects on magnesium formability will help reduce the cost of these products. In this thesis, the microstructural factors that affect the formability of rolled and extruded magnesium sheet were compared. It was found that the degree of dynamic recrystallization was the factor that controlled elongation. Dynamic recrystallization produced a finer grain size, which resulted in a transition in deformation mechanism from dislocation slip to grain boundary sliding.

Digital image correlation was used to study local stresses during tensile deformation, and to determine if magnesium satisfies Considère's criterion before failure. The results indicated that local stresses developed during deformation satisfied Considère's criterion, although the global strains were lower than the theoretical predictions.

Acknowledgements

First, I would like to thank my supervisor, Dr. Wilkinson, for his assistance with my project. I would also like to thank Dr. Verma at GM for providing the materials used in this study. The assistance of the following people at McMaster University is also appreciated:

- Dr. Bruhis and R. Lemmon for DIC and mechanical testing expertise
- Dr. Britten and Dr. Hu for XRD testing and analysis
- D. Culley and C. Butcher for metallography
- Dr. Koprich for SEM help
- J. Rodda for chemical analysis

Discussions with Dr. Weck and A. Hosokawaa in my research group were also very helpful. Finally, the support and prayers of my family and friends were very much appreciated.

Table of Contents

List of Figures

List of Tables

1. Introduction

The use of magnesium alloys has become more common in mechanical design. This is due to magnesium's low density, high strength-to-weight ratio, and high specific stiffness. These attributes can result in high performance and reduced energy consumption. The automotive industry has become a major user of magnesium components. However, use of magnesium sheet products is quite limited, due to difficulties in producing cost effective components. This lack of formability is attributed to magnesium's HCP crystal structure. Any sheet currently produced is formed at elevated temperatures, making magnesium parts relatively expensive. Knowledge of the microstructural effects on magnesium formability will help reduce the cost of these products.

This thesis will help develop an understanding of what microstructural features influence the formability of rolled and extruded magnesium sheet alloys at elevated temperatures. A literature review of the mechanical behaviour of magnesium alloys is presented in chapter 2. The particular objectives of the thesis are stated in chapter 3. The experimental procedures used in this study are described in chapter 4. Chapter 5 presents the results of the research. A discussion of the results is presented in chapter 6. The final chapter contains the conclusions reached.

2. Literature Review

This chapter contains a literature review on the mechanical behaviour of Mg alloys related to this research. Magnesium's crystal structure will be discussed, as well as its associated deformation mechanisms. The roles of grain size and texture on deformation will also be discussed. Elevated temperature deformation will be reviewed, along with the role of dynamic recrystallization. Strain localization and tensile instability will be discussed.

2.1 Magnesium Alloy Nomenclature

A standard system for naming magnesium alloys was adopted in 1948 by the American Society for Testing and Materials (ASTM). An example is AZ91E-T6. The two letters at the beginning of the designation refer to the principal alloying elements, in this case aluminum (A) and zinc (Z). The first two numbers give the rounded weight percentages of the alloying elements; 9 wt% Al, 1 wt% Zn. The third letter, E in this case, indicates that this alloy was the fifth one standardized with 9 wt% Al and 1 wt% Zn. The final grouping indicates the temper designation. In this example, T6 indicates that the alloy has been solution heat treated and artificially aged (Housh et al (1990)). A table with letters and their corresponding element is given below.

Table 2.1 Magnesium alloy nomenclature (Housh et al (1990)).

Letter	Element	Letter	Element	Letter	Element	Letter	Element
A	Aluminum	F	Iron	M	Manganese	S	Silicon
B	Bismuth	G	Magnesium	N	Nickel	T	Tin
C	Copper	H	Thorium	P	Lead	W	Yttrium
D	Cadmium	K	Zirconium	Q	Silver	Y	Antimony
E	Rare Earth	L	Lithium	R	Chromium	Z	Zinc

2.2 Magnesium Crystallography

Magnesium has a hexagonal close packed (HCP) structure with a *c/a* ratio of 1.623, which is slightly less than the ideal ratio of 1.633. This ratio affects the deformation modes of the material. In crystals where *c/a* is greater than 1.633, $(10\bar{1}2)$ twinning is activated by compression parallel to and/or tension perpendicular to the *c*-axis. Alternatively, when *c/a* is less than ideal, the opposite holds: tension parallel to and/or compression perpendicular to the *c*-axis causes twinning (Partridge (1967)). Also, prismatic slip is dominant at low temperatures in metals with low *c/a* ratios, such as titanium and zirconium. Magnesium's primary slip mode at low temperatures is basal slip (Murty (2003)).

The important directions and planes in HCP metals are displayed in Figure 2.1. Three important zone axes exist in HCP metals: <0001>, <10$\bar{1}$0>, and <11$\bar{2}$0>. {hkl0} planes intersect the basal plane at 90° These planes are further broken up into prism planes of type I and type II. {1$\bar{1}$00} planes are type I, while {1$\bar{2}$1n} planes are type II. {$hkln$}, n ≠ 0 are called pyramidal planes (Partridge (1967)).

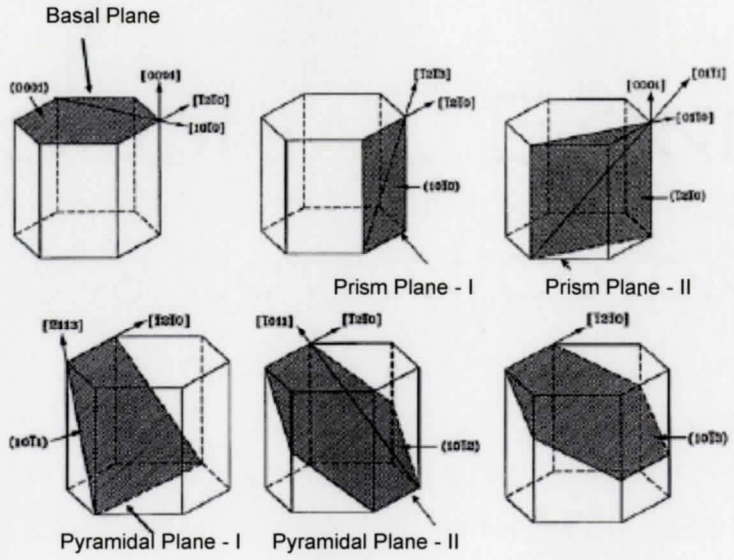

Figure 2.1 Important directions and planes in HCP metals (Bhattacharya, 2006).

2.3 Deformation Mechanisms in Magnesium

2.3.1 Slip

Slip is defined as plastic deformation produced from dislocation motion. Slip will occur most easily on planes with the densest atomic packing in directions with the highest linear atomic density (Callister (2003)). In magnesium, the close packed directions are

the six $<11\bar{2}0>$ directions, with a Burgers vector denoted $<a>$, along the basal plane (Partridge (1967)). At room temperature, basal slip is the dominant slip mode, as it has the lowest critical resolved shear stress (CRSS) (Yoshinaga and Horiuchi (1963)). Other reported slip systems are $(10\bar{1}0)$ prism slip, $(10\bar{1}1)$ pyramidal slip and $(11\bar{2}2)$ type II pyramidal slip. The amount of slip in these systems increases as temperature increases, due to a drop in the CRSS (Wonsiewicz and Backofen (1967)).

The Taylor criterion states that five independent slip systems are necessary for an arbitrary deformation. Magnesium has only two independent slip systems, along $<11\bar{2}0>$ in the basal plane. Therefore, additional deformation mechanisms are required to accommodate strain along the *c*-axis (Kelley and Hosford (1968)). Twinning or slip on type II pyramidal planes $\{11\bar{2}2\}<11\bar{2}3>$, (with a Burgers vector called $<c+a>$) are mechanisms that allow for *c*-axis deformation. $<c+a>$ slip alone has five independent slip systems, satisfying the Taylor condition (Partridge (1967)). At elevated temperatures, the CRSS for non-basal slip decreases significantly, as illustrated in Figure 2.2. This increase in the number of available slip systems helps explain the increase in ductility observed in magnesium alloys at these temperatures (Yoshinaga and Horiuchi (1963)).

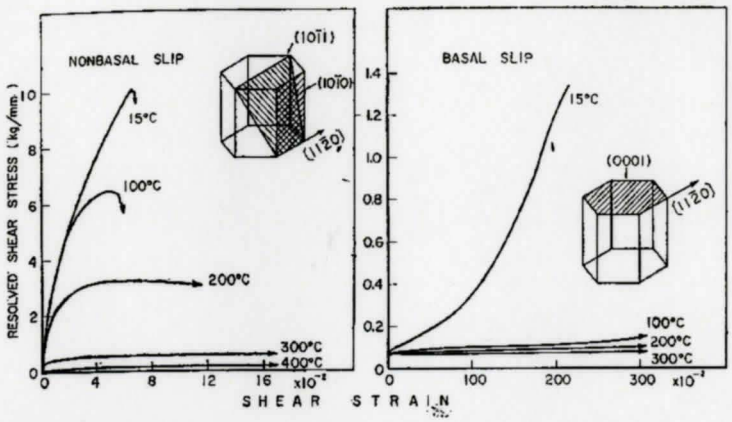

Figure 2.2 CRSS for basal and non-basal slip at room and elevated temperatures (Yoshinaga and Horiuchi, 1963).

2.3.2 Twinning

Twinning is a deformation mechanism that involves part of a metal's crystal lattice reorienting due to an applied shear stress to become a mirror image of the original, untwinned lattice. Atoms in the twinned portion of the lattice move a distance proportional to their distance from the twin plane. The line of symmetry between the deformed and undeformed parts of the lattice is called the twin plane. Twins formed during a plastic deformation process are termed mechanical twins (Dieter (1986)). Figure 2.3 provides a visual description of twinning.

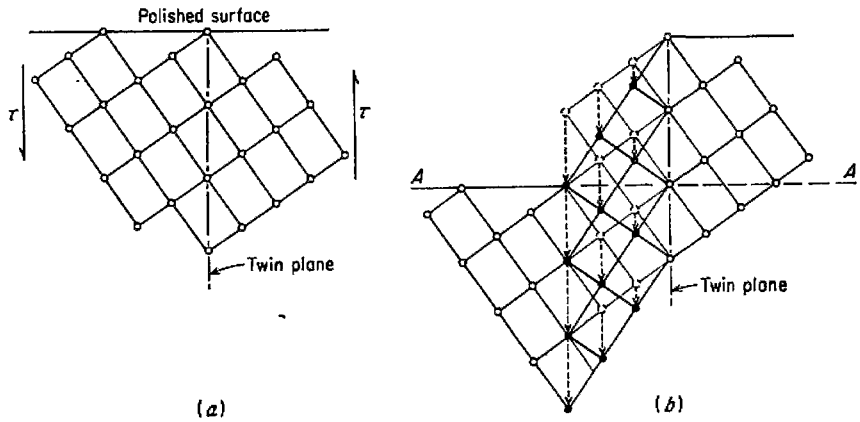

Figure 2.3 Graphical representation of twinning. Part a) is undeformed, b) is deformed. White dots represent atoms which have not moved. Black dots represent the final position of atoms that have moved during the twinning process (Dieter, 1986).

The dominant twinning mode in magnesium is $\{10\bar{1}2\}\langle 10\bar{1}1\rangle$. When the applied stress is parallel to the basal plane, this type of twin is only possible when the stress is compressive. Tensile stresses applied perpendicular to the basal plane will also produce $\{10\bar{1}2\}\langle 10\bar{1}1\rangle$ twins, compressive stresses along this plane will not. This is a geometrical consequence of magnesium having a *c/a* ratio below 1.633 (Emley (1966)). Reed-Hill and Robertson (1957) reported a CRSS of 2 MPa at room temperature for this type of twinning. Twinning has also been reported to occur on $\{10\bar{1}1\}$, $\{10\bar{1}3\}$, and $\{30\bar{3}4\}$ planes (Reed-Hill and Robertson (1957)). $\{10\bar{1}1\}$ twinning has a much greater CRSS, with values between 76-154 MPa, depending on the direction of the applied stress (Wonsiewicz and Backofen (1967)). The magnitude of the twinning shear is relatively small (0.131 in magnesium for $\{10\bar{1}2\}\langle 10\bar{1}1\rangle$ twins). However, twinning can reorient

the crystal lattice of grains unfavourably oriented for slip to positions more favourably oriented (Partridge (1967)).

2.3.3 Grain Boundary Sliding

Grain boundary sliding (GBS) is a deformation mode in which grains slide past one another, with very little shape change in the grains. The grains move past each other to increase their number in the direction of the applied tensile stress, resulting in permanent deformation. This decreases the number of grains in the width and thickness of the material as they flow in the direction of the applied stress, resulting in thinning. GBS plays an important role in superplastic forming operations (Langdon (1994b)).

GBS must be accommodated by a secondary mechanism, or cavities will form at grain boundary triple points as grains slide past one another. Several mechanisms have been proposed: grain boundary migration, dislocation slip, diffusional flow, and recrystallization (Nieh et al. (1997)). Two authors have reported dislocation slip accommodated by GBS in magnesium alloys (Mabuchi et al. (1999), Perez-Prado et al. (2004)).

Grain boundary sliding is believed to be the dominant deformation mode in superplastic forming (Langdon (1994a)). Superplasticity, which generally takes place at elevated temperatures and/or low strain rates, has been seen as a possible solution to magnesium's poor room temperature formability (Bussiba et al. (2001)). The strain rate

for superplasticity is inversely proportional to the square of the grain size (see equation 2.1 below). Thus, the smaller the grain size, the larger the strain rate can be (Nieh et al. (1997)).

High strain rate superplasticity (HSRS) is defined as superplasticity taking place at strain rates greater than or equal to 10^{-2} s^{-1} (Watanabe et al. (1999a)). Figure 2.4 shows the effect of strain rate on elongation in some magnesium alloys. Low temperature superplasticity (LTS) takes place below $0.5T_m$, where T_m is the absolute melting temperature. Both LTS and HSRS are attractive for commercial applications, as the shorter time or lower temperature required to produce parts would lower costs (Jin et al. (2005)).

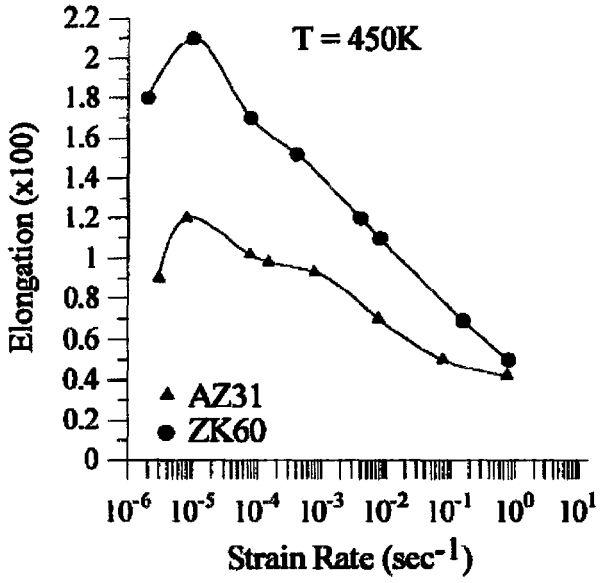

Figure 2.4 Effect of strain rate on elongation to failure in two magnesium alloys (Bussiba et al., 2001).

Since small grain sizes are considered optimal for superplasticity, many attempts have been made to refine the grain size of magnesium alloys. These grain refining processes include equal channel angular pressing (ECAP) (Kim et al. (2003), Miyahara et al. (2006)), cold rolling and annealing (Itoh et al. (2004)), powder metallurgy methods (Mabuchi et al. (2001)), and large strain hot rolling (Perez-Prado et al. (2004)). Wei et al. (2003) achieved an elongation of ~ 170% in an AZ91 alloy hot rolled to 11 μm, at a strain rate of 1 s^{-1} and a temperature of 350°C. Watanabe et al. (2002) achieved a ductility of 164% in a ZK60 alloy at a strain rate of $1X10^{-2}$ s^{-1} at 200°C. This alloy had a grain size of 1.4 μm after ECAP.

Grain growth at high temperatures can inhibit superplasticity in magnesium alloys. Very coarse grains in a fine grained matrix can result in microcracking at the coarse/fine grain interface. This leads to premature failure. Hence, grain size distribution is a factor in magnesium formability (Bussiba et al. (2001)).

Two phase microstructures are often considered to enhance superplasticity. The presence of a second phase prevents grain growth at the elevated temperatures at which superplasticity normally occurs. Small second phase particles can pin grain boundaries, preventing them from growing. A fine dispersion of the second phase is considered optimal. Increasing the amount of the second phase will further prevent grain growth, as long as the phase is uniformly distributed in the alloy. However, hard particles in a soft matrix can act as stress concentration sites, resulting in cavity

formation at the particle/matrix interface (Nieh et al. (1997)). Marya et al. (2006) processed an AZ31 alloy to obtain $Mg_{17}Al_{12}$ precipitates. The alloy with precipitates had an elongation approximately 33% greater than that of the base system. Watanabe et al. (2001a) formed precipitates in a WE43 alloy with a 2 μm grain size. They reached a 1000% elongation at 400°C and a strain rate of 1×10^{-4} s^{-1}. The $Mg_{11}NdY_2$ precipitates hindered grain growth at the test temperature.

Attempts have been made to determine if GBS occurs at room temperature in magnesium alloys. Hauser et al. (1955) determined that GBS accounted for 4% of the total strain in a pure magnesium extrusion. GBS was also observed in samples tested at 78 K (Hauser et al. (1956)). However, Gifkins and Langdon (1965) concluded that GBS does not take place in magnesium at room temperature. Their samples had grain sizes between 94 and 313 μm. More recently, Ohyama et al. (2003) found that GBS did occur at room temperature in an 8 μm AZ31 alloy. GBS was also reported to be the dominant deformation mode during compression tests of 45 nm pure magnesium (Hwang et al., 2001). It would seem that small grain sizes allow for GBS at room temperature, although the contribution of GBS to total strain is low.

Based on creep equations developed by Mukherjee et al. (1969), Watanabe et al. (2001b) have proposed a constitutive equation for superplasticity in magnesium alloys:

$$\dot{\varepsilon} = 1.8\times10^{6}\left(\frac{Gb}{kT}\right)\left(\frac{b}{d}\right)^{2}\left(\frac{\sigma}{G}\right)^{n} D_{eff} \qquad (2.1)$$

where $\dot{\varepsilon}$ is the strain rate, G the shear modulus, b the Burgers vector, k is Boltzmann's constant, T the absolute temperature, d the grain size, σ the flow stress, and D_{eff} the effective diffusion coefficient. Sherby et al. (1981) proposed the following equation for D_{eff}:

$$D_{eff} = D_L + x\left(\frac{\pi}{d}\right)\delta D_{gb} \tag{2.2}$$

where D_L and D_{gb} are the lattice and grain boundary diffusion coefficients, x is a constant equal to 1.7×10^{-2} for magnesium alloys (Watanabe et al. (2001b)), and δ is the grain boundary width.

2.4 Factors Influencing Formability

2.4.1 Temperature

The ductility of a metallic material generally increases as the temperature is increased. Magnesium is no exception. The ductility increase is due to an increased number of available deformation modes. At higher temperatures, the CRSS for non-basal slip quickly decreases, increasing the number of available slip systems (see Figure 2.2). Note that the CRSS for non-basal slip approaches the CRSS for basal slip as the temperature is raised (Jager et al. (2004)). The contribution of grain boundary sliding to total strain is increased at elevated temperatures. This was due to an enhancement of the accommodation processes; grain boundary diffusion and lattice diffusion in this case (Li et al. (2005)).

Figure 2.5 shows the effect of temperature on the flow properties of a hot rolled AZ31 alloy. Ductility increases as temperature increases. Work hardening is only present at room temperature and 100°C. The flow stress decreases as temperature increases, with a steady flow stress developing at 200°C, indicating superplasticity (Jager et al. (2004)).

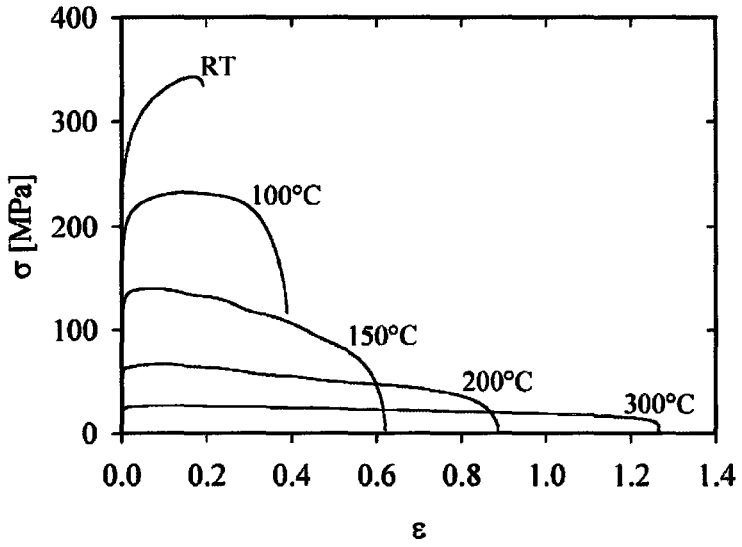

Figure 2.5 Effect of temperature on flow curves (Jager et al. (2004)).

Mechanical twinning is believed to be athermal. The stress required to activate twinning is insensitive to temperature (Meyers et al. (2001)). However, twinning in magnesium alloys is much more prevalent during low temperature (<200°C) deformation. The formability of magnesium alloys in this temperature region is not good, and formability increases at temperatures above 200°C. It has been shown (Figure 2.6) that the volume fraction of twins decreases as forming temperature increases. Decreasing the amount of twinning resulted in greater ductility (Jain and Agnew (2007)).

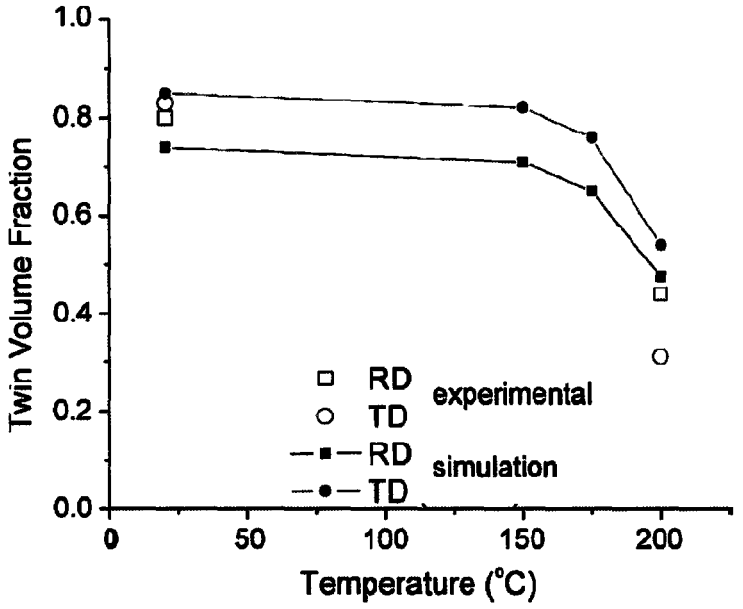

Figure 2.6 Twin volume fraction plotted against temperature at a strain of 0.11 (Jain and Agnew (2007)).

2.4.2 Grain Size

Grain size plays a major role in determining the formability of a magnesium alloy. Smaller grain sizes increase ductility (Chapman & Wilson (1962-3), Wilson (1970), Mukai et al. (2001)). Wang et al. (2005) also show this in extrusions of AZ31 tested at room temperature. The grain size was manipulated by adjusting the extrusion temperature. As the grain size decreased, the total elongation increased (see Figure 2.7). Mukai et al. (2001a) attributed the increase in ductility to a lack of cracking at twin boundaries in a fine grained material. Watanabe et al. (2001c) have shown that smaller grain sizes increase the strain to failure at elevated temperatures. This was likely due to an increased incidence of GBS.

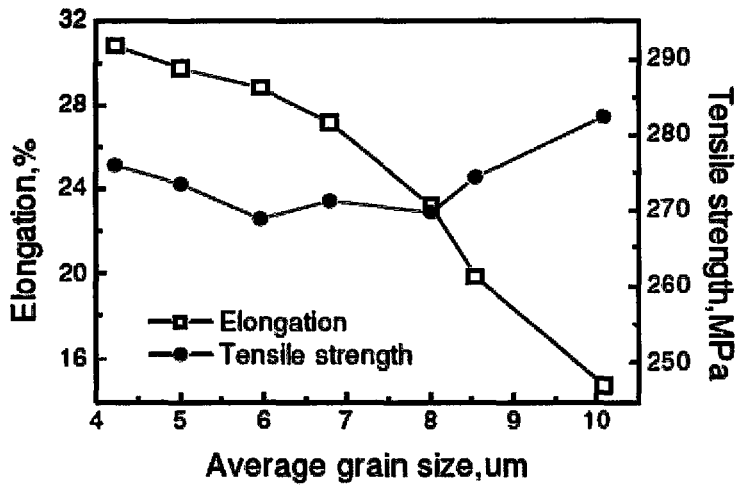

Figure 2.7 Influence of grain size on room temperature ductility (Wang et al. (2005)).

The strain hardening rate is also influenced by grain size. del Valle et al. (2006) have examined this behaviour in an AZ31 alloy. Samples were large strain hot rolled to produce a fine grain size, and then annealed to produce a larger grain size. The strain hardening rates decreased as grain size was reduced (see Figure 2.8). A change in deformation mode to GBS was postulated to explain this behaviour. However, samples with higher work hardening rates had higher elongations.

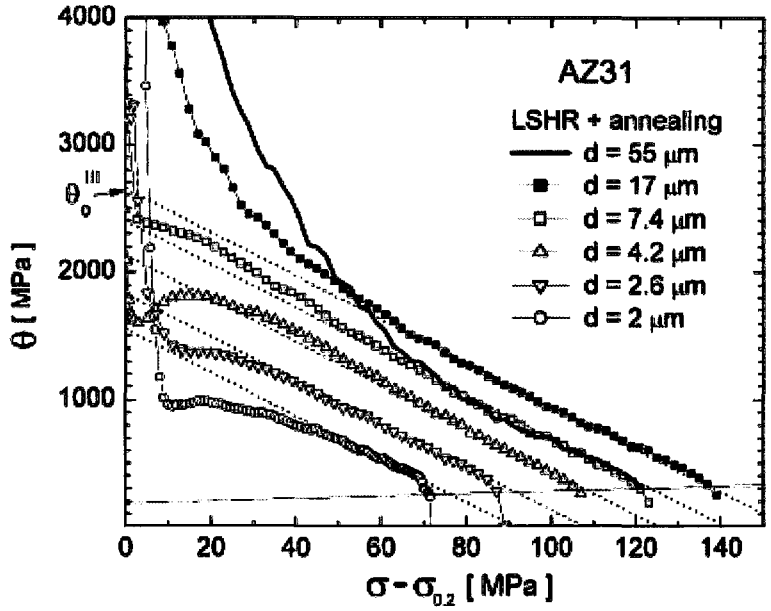

Figure 2.8 Work hardening rates of AZ31 at different grain sizes (del Valle et al. (2006)).

Smaller grain sizes also inhibit twinning (Lahaie et al. (1992), Barnett et al. (2004), Wang et al. (2007)). This fact is illustrated in Figure 2.9, where twin volume fraction is plotted against grain size in tension and compression. Also of note is that twinning is more prevalent in compression than in tension. It is generally believed that twinning results from stress concentrations at grain boundaries. Thus, larger grains will develop more stresses at their grain boundaries, leading to deformation twinning (Wang et al. (2007)).

A transition from twinning to slip dominated flow in compression tests of AZ31 can be observed in Figure 2.10 from the work of Barnett et al. (2004b). Materials with grain sizes between 8-22 μm exhibited a sigmoidal-shaped flow curve, which is

indicative of twinning in compression tests. When the grain size was reduced to 4 μm, the flow curves followed a power-law shape. Twinning dominated flow produces a higher strain hardening rate, as the twin boundaries act as additional obstacles to dislocation motion. The transition in flow behaviour was believed to occur when the macroscopic stress required to initiate twinning was equal to the stress required for <*c*+*a*> slip (Barnett (2003a)). The stress to initiate twinning increases as the grain size decreases. The stress required for basal slip increases at a slower rate, meaning that slip becomes easier than twinning at small grain sizes (Meyers et al. (2001)).

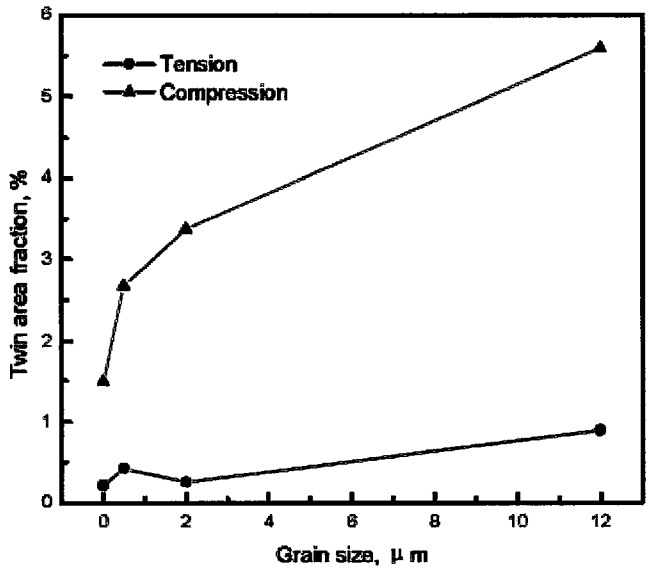

Figure 2.9 Twin area fraction versus grain size in an extruded AZ31 alloy (Wang et al. (2007)).

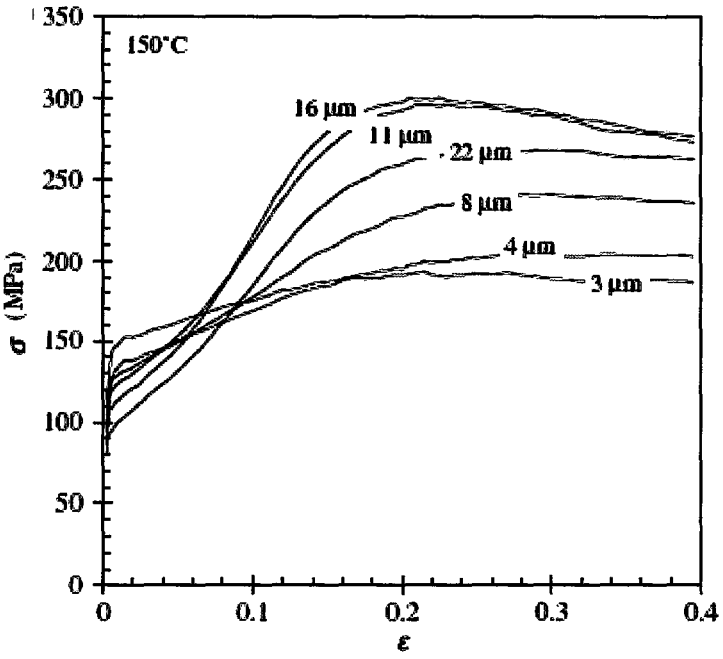

Figure 2.10 Compression tests of AZ31, indicating a transition from twinning to slip dominated flow as the grain size is reduced (Barnett et al. (2004b)).

The Hall-Petch equation (Hall (1951), Petch (1953)) can be used to model the yield strength (σ_y) of many materials:

$$\sigma_y = \sigma_0 + kd^{-1/2} \tag{2.3}$$

where d is the grain size, σ_0 is a material constant called the friction stress, representing the material's resistance to dislocation motion, and k is another constant called the strength coefficient. Many researchers have found that magnesium and its alloys satisfy this relationship (Mukai et al. (2001a), Mabuchi et al. (2001b), Ono et al. (2003), Ono et al. (2005), del Valle et al. (2006), Kim et al. (2007), Wang et al. (2007)). Values of k ranged from 142.531 MPa·µm$^{1/2}$ (Wang et al. (2007)) to 290.93 MPa·µm$^{1/2}$. Ono et al. (2003) found that the Hall-Petch equation was satisfied at low and high temperatures in

pure magnesium (Figure 2.11). Others have found that no correlation exists. Texture effects were said to dominate the flow behaviour in these cases (Lim et al. (2006)).

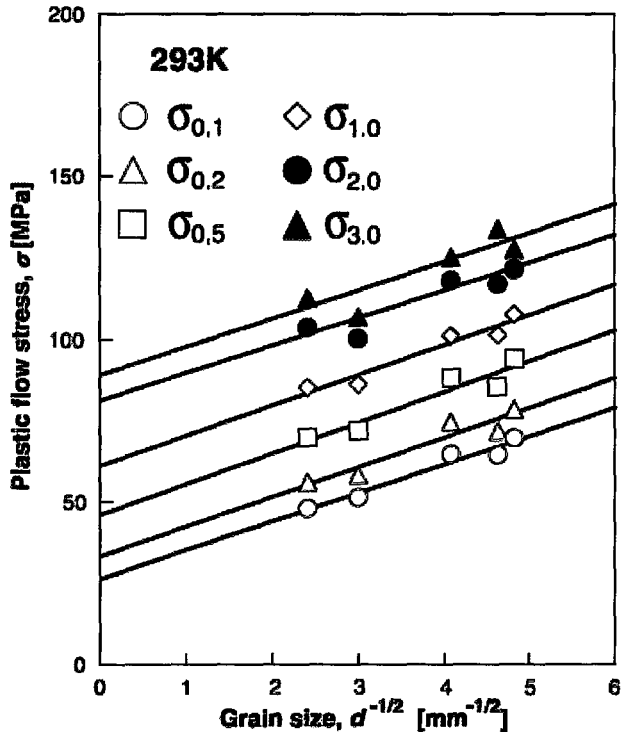

Figure 2.11 Hall-Petch curves in pure magnesium at low and high temperatures (Ono et al. (2003)).

2.4.3 Texture

Due to the anisotropy of the HCP lattice and the variety of deformation mechanisms, texture is a critical component in determining magnesium's formability. Thus, controlling texture during primary processing (rolling or extrusion, for example) will dictate the formability of the magnesium piece during secondary processing. A

strong basal texture usually results from these processes, resulting in poor room temperature formability (Watanabe et al. (2007)).

Yi et al. (2006) examined the role of crystallographic orientation on deformation mechanisms. They found that when the *c*-axis was perpendicular to the applied stress direction, plastic deformation began with basal <*a*> slip. Eventually the stress reached high enough values that prismatic <*a*> and pyramidal <*a*> slip systems were activated. These samples had high yield strengths. When the *c*-axis was 45° from the stress axis, basal <*a*> slip was dominant, and the samples had a low yield stress. $\{10\bar{1}2\}$ twinning had a large influence on samples with the *c*-axis parallel to the stress axis. Some basal and non-basal <*a*> slip was also observed under this condition.

Random textures have been found to improve ductility when compared to basal textures (Mukai et al. (2001b), Huang et al. (2005), Gehrmann et al. (2005)). Mukai et al. showed this by ECAPing an extruded AZ31 alloy to randomize the texture. This material was subsequently annealed to achieve the same grain size as the original extruded sample. The effect of the ECAP process on texture can be seen in Figure 2.12. ECAPing almost doubled the strain to failure from approximately 0.24 to 0.47.

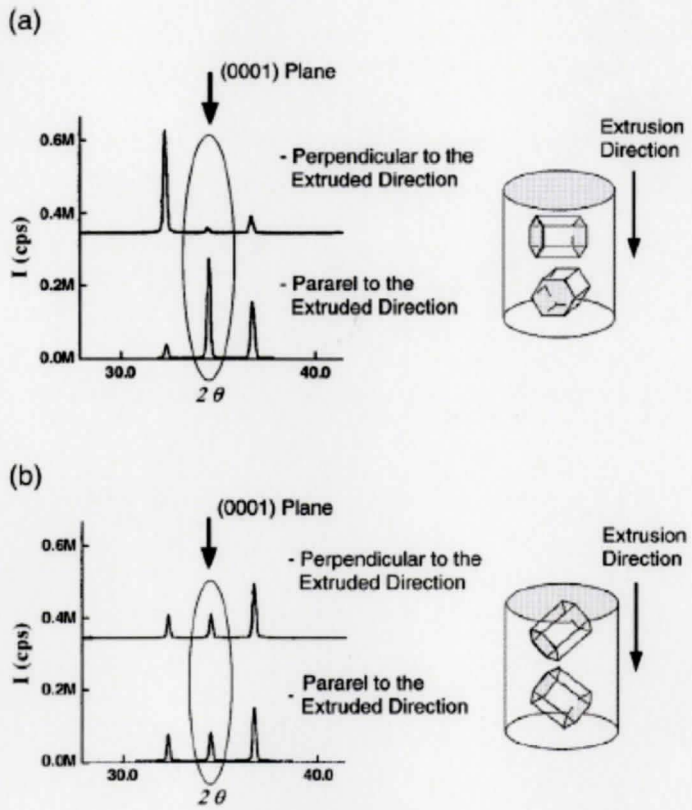

Figure 2.12 Texture randomization a) as-extruded and b) ECAPed material (Mukai et al. (2001)).

Kim et al. (2003) have found that texture softening had a larger impact on yield strength than grain refinement. Figure 2.13 illustrates this. Here, the material represented by curve 0 has a grain size of 400 μm, curve two 34 μm, and curve eight 23 μm. The grain size for curve 1 was unreported. ECAP was used to refine the grains and homogenize the texture. The number on each curve represents the number of ECAP passes. The yield strength of the 23 μm material was 125 MPa, while that of the 400 μm material was 154 MPa. The as-received extruded sheet had a strong basal texture, which was broken down during ECAP Under similar microstructural conditions, Huang et al. (2005) reported that basal slip occurred when the basal plane was inclined from the stress

axis. When the basal plane is parallel or perpendicular to the stress axis, the Schmid factor is ~0. When the basal plane is inclined with respect to the stress axis, the Schmid factor is higher, and basal slip can take place. This resulted in a lower yield strength.

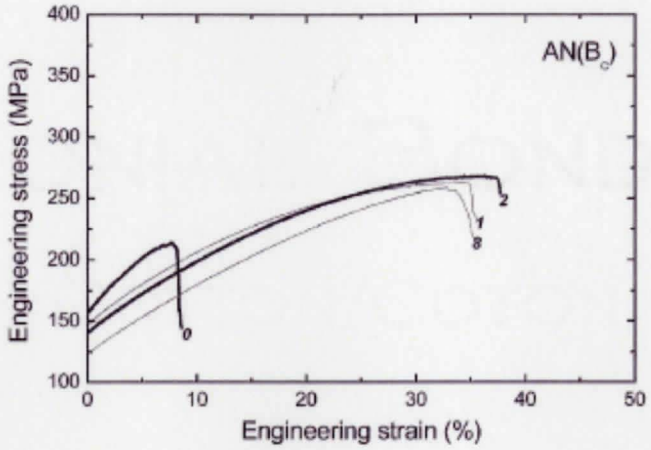

Figure 2.13 Effects of randomized texture on flow properties (Kim et al. (2003)).

Micro-alloying with rare earth elements has been shown to weaken the texture in magnesium alloys (Bohlen et al. (2007), Stanford and Barnett (2008)). After equating the grain size in each material to 30 μm, Stanford and Barnett found that alloying with Al, Sn, Gd, and La improved the formability compared to a pure Mg alloy. The elongation to failure increased by at least 20% for each alloying element. This improvement was attributed to weaker textures better aligned for basal slip. It was also found that alloying with Ca formed a stronger basal texture, and reduced formability.

Perez-Prado and Ruano (2002) have studied annealing textures in AZ31 They found that a $(11\bar{2}0)$ texture developed upon annealing at 520°C for 19 hours. Other

authors have reported a weakening of a basal texture after annealing Mg sheet alloys (Barnett, 2003b, Kim et al., 2005, Jager et al., 2006). In contrast, Yang et al. (2005) report that annealing and grain growth produced very little texture change in AZ31. Clearly, more work is needed to understand annealing textures in magnesium alloys.

2.5 Recrystallization

Recrystallization is the process encompassing the nucleation and growth of new, strain free grains. Recrystallization determines the grain size of wrought magnesium. Since the effects of grain size on magnesium are significant (see section 2.3.2), an understanding of recrystallization in magnesium is critical (Barnett (2003b)). Dynamic recrystallization (DRX) has been seen as a potential tool with which to control the texture of magnesium (Backx and Kestens (2005)).

Several nucleation mechanisms have been proposed to operate in magnesium: bulging (Tan and Tan (2003)), twinning (Sitdikov et al (2003)), subgrain rotation (Ion et al. (1982)), and particle stimulated nucleation (Mackenzie et al. (2004)). Sitdikov et al. (2003) have studied nucleation by twinning during elevated temperature compression. They found that the new grains nucleate at twin-twin intersections, or through rearrangement of dislocations within the twin lamellae. These nuclei then grow into high angle boundaries. The grain boundaries migrate until new grains are formed.

Nucleation by grain boundary bulging occurs when the density of dislocations entering the grain boundary exceeds the absorption capacity of the grain boundary. Dislocations of opposite signs do not annihilate each other. These dislocation pileups produce stress concentrations at the grain boundaries, which lead to grain boundary serrations. Dislocations near these serrations reduce the stress by forming low angle boundaries and cell structures, which result in subgrain formation. As deformation proceeds, the misorientation angle between the grain and subgrain increases, resulting in new high angle grain boundaries (Tan and Tan (2003)).

Grain boundary bulging often leads to a "necklace" type microstructure, where a relatively large, unrecrystallized grain will be surrounded by small, recrystallized grains. Subsequent necklaces will be formed at the parent grain/original necklace interface, until the parent grain is consumed. Ponge and Gottstein (1998) have studied this in Ni_3Al. They found that the first necklace layer has a similar orientation to the parent grain. However, each subsequent necklace layer had a higher degree of misorientation compared to the original grain. This discrepancy was believed to be a result of either the nucleation mechanism changing to twinning, or to grain rotation during deformation. Necklace type recrystallization has been reported in magnesium alloys by several authors (Barnett et al. (2004a), Backx and Kestens (2005), Huang et al. (2005), Al-Samman and Gottstein (2008)).

Both test conditions and microstructural factors influence recrystallization in magnesium. Huang et al. (2005) showed that the fraction of recrystallized grains, X_v, increased with decreasing grain size, as shown in Figure 2.14. Necklace type recrystallization was reported. Since new grains nucleated at grain boundaries in this case, a larger grain boundary area led to more recrystallization. Nucleation by twinning was also observed in a large grained (90 μm) sample. Despite the additional nucleation mechanism, the fine grained (22 μm) sample had a larger X_v values. The smaller grain size also increased the misorientation angle of the DRX grain boundaries. The misorientation angles also plateau, which differs from the earlier work in Ni_3Al (Ponge and Gottstein (1998)).

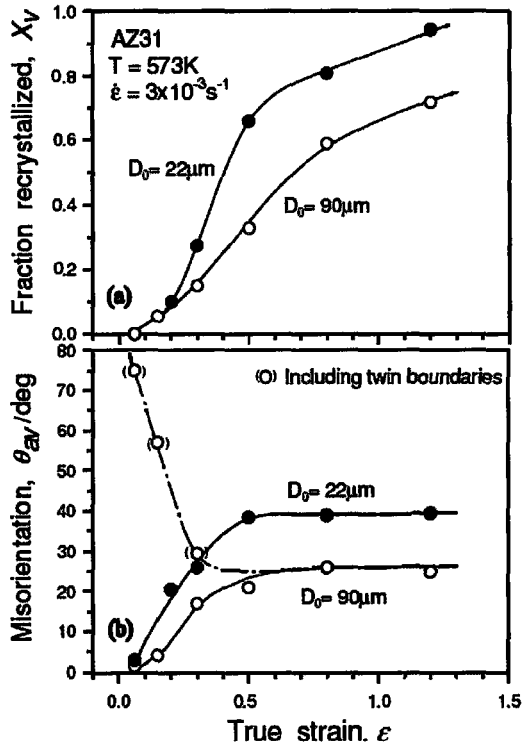

Figure 2.14 Initial grain size versus fraction recrystallized during 300°C compression tests (Huang et al. (2005)).

Backx and Kestens (2005) found that a lower strain rate during compression resulted in more randomly oriented DRX grains (Figure 2.15). The lower strain rate produced a larger fraction of DRX grains (58%) than the higher strain rate (42%). These authors have also studied the influence of temperature. Figure 2.16 shows that a higher test temperature at a constant strain rate produced more randomly oriented DRX grains. It was also found that tests at 250°C resulted in 50% recrystallization, while tests at 200°C only resulted in 42% recrystallization at a strain of 0.5.

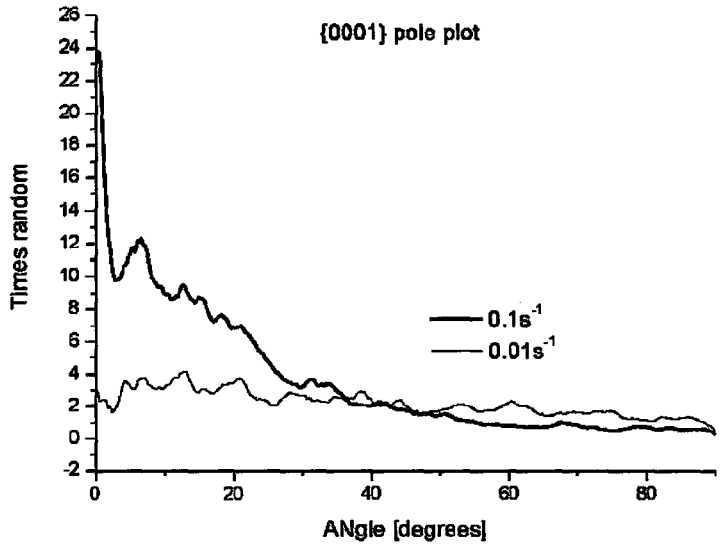

Figure 2.15 Influence of strain rate on DRX grain orientation (Backx and Kestens (2005)).

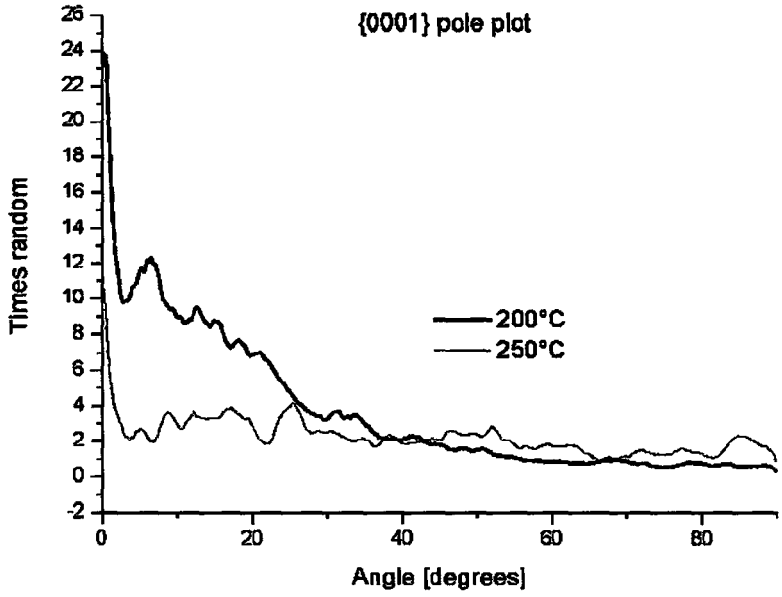

Figure 2.16 Influence of temperature on DRX grain orientation (Backx and Kestens, (2005)).

DRX has been reported to improve formability (Mohri et al. (2000), Backx and Kestens (2005), Al-Samman and Gottstein (2008), Vespa et al. (2008)). Al-Samman and Gottstein (2008) tested AZ31 in compression at 200°C and $10^{-2}s^{-1}$, and observed a brittle outside but ductile inside of the sample. Microstructural investigation revealed that the sample's interior had recrystallized, while the outer part did not. This phenomenon was attributed to an inhomogeneous strain distribution during the test. Part of this ductility increase was attributed to a more random DRX texture. Mohri et al. (2000) reported a transition in deformation mode after a strain of 0.1. After DRX, GBS became the dominant deformation mode, and increased the elongation to failure.

2.6 Tensile Instability

Necking begins at the point of maximum load in a tensile test. During the test, the metal will undergo strain hardening after yielding, which increases the material's load carrying capacity. Simultaneously, the tensile sample will thin, reducing the cross sectional area, and reducing the sample's ability to carry a load. When the increase in load carrying capacity due to strain hardening equals the decrease due to thinning, necking will begin in the sample. The instability condition is defined as $dP = 0$, where P is the load. Combining this with the constancy of volume relationship, equation 2.1 can be defined:

$$\frac{d\sigma}{d\varepsilon} = \sigma \tag{2.4}$$

where σ is the true stress and ε is the true strain. Thus, the point of instability can be defined as the point where the strain hardening rate is equal to the true stress (Dieter (1986)).

The Holloman equation (2.2) can be used to model the flow curve of many metals in the region of uniform plastic deformation:

$$\sigma = K\varepsilon^n \tag{2.5}$$

where K is the strength coefficient, and n is the strain hardening exponent. Taking the derivative of σ with respect to ε, it can be shown that:

$$\frac{d\sigma}{d\varepsilon} = n\left(\frac{\sigma}{\varepsilon}\right) \tag{2.6}$$

Combining equations 2.4 and 2.6, the relationship $\varepsilon = n$ at the point of necking can be determined. This relationship, called Considère's criterion, only works if the material obeys the Holloman equation (Dieter (1986)).

If a material fails before the flow stress equals the work hardening rate, failure is said to be premature. The material's capacity for stable flow has not been met. Often this is due to strain localization, which has been reported in magnesium by several authors (Kelley and Hosford (1968), Gehrmann et al. (2005), Barnett (2007), Al-Samman and Gottstein (2008)). Kelley and Hosford (1968) reported that regions with grains oriented for basal slip exhibited larger strains. Al-Samman and Gottstein (2008) report shear bands and shear cracks in room temperature compression tests that caused a noticeable loss in strength after the peak load was reached. This occurred after the twinning capacity was exhausted, and dislocation-twin interactions resulted in a high work hardening rate. Gehrmann et al. (2005) reported similar results during tests performed at 100°C and 200°C. Barnett (2007) has observed twins joining cooperatively to form shear bands near the fracture point of an AZ31 alloy tested in tension at room temperature (Figure 2.17). It was found that twinning can cause strain localization leading to premature failure.

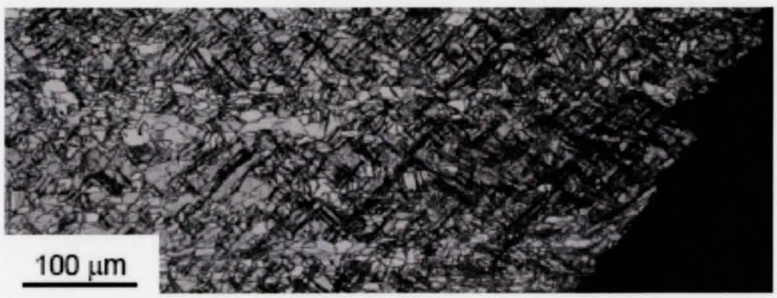

Figure 2.17 Twinning and shear bands in AZ31 at fracture (Barnett (2007)).

Bhattacharya (2006) found that single crystals of pure magnesium do not satisfy Considère's criterion before fracture. However, some fine-grained (13-30 μm) polycrystalline samples did. It was believed that strain localization due to non-basal slip or twinning caused premature failure. Luo and Sachdev (2007) reported that Considère's criterion was not met in AZ31 and AM30 alloys tested at 177°C or below (Figure 2.18). No necking was observed in these samples, and it was suggested that work hardening effectively distributed plastic deformation. At 204°C, Considère's criterion was satisfied for AM30 but not AZ31. The higher formability of AM30 in this study was attributed to its' higher work hardening rate. DRX at the grain boundaries of these samples led to local softening and plastic instability. del Valle et al. (2006) reported that AZ31 and AM60 alloys tested at room temperature "almost " reached the instability point. This was true regardless of the grain size or texture of the material.

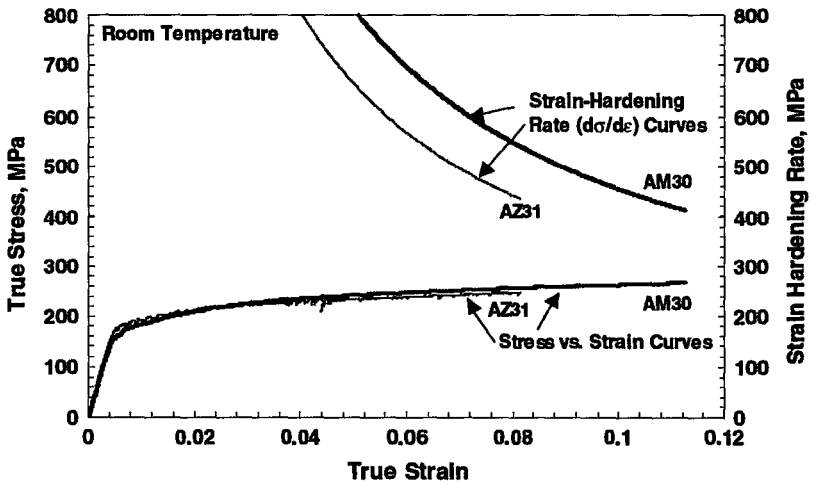

Figure 2.18 True stress - true strain curves and strain hardening rates for AZ31 and AM30 tested at room temperature (Luo and Sachdev (2007)).

2.7 Comparing Rolled and Extruded Magnesium Alloys

Several authors have compared rolled magnesium sheet with extruded rod materials (Ishihara et al. (2007), Xue et al. (2005), Watanabe et al. (2000)). However, very little work has been done comparing the mechanical properties of rolled and extruded magnesium sheet alloys. Song et al. (2003) extruded an AZ31 slab to 5 mm thickness, and then hot rolled this by 10% and to a thickness of 1 mm. The tensile properties of this material were tested after each thermomechanical step. The flow curves they obtained are shown in Figure 2.19. Thermomechanical processing increased the yield strength and ductility. This was explained by recrystallization producing finer grains after hot rolling.

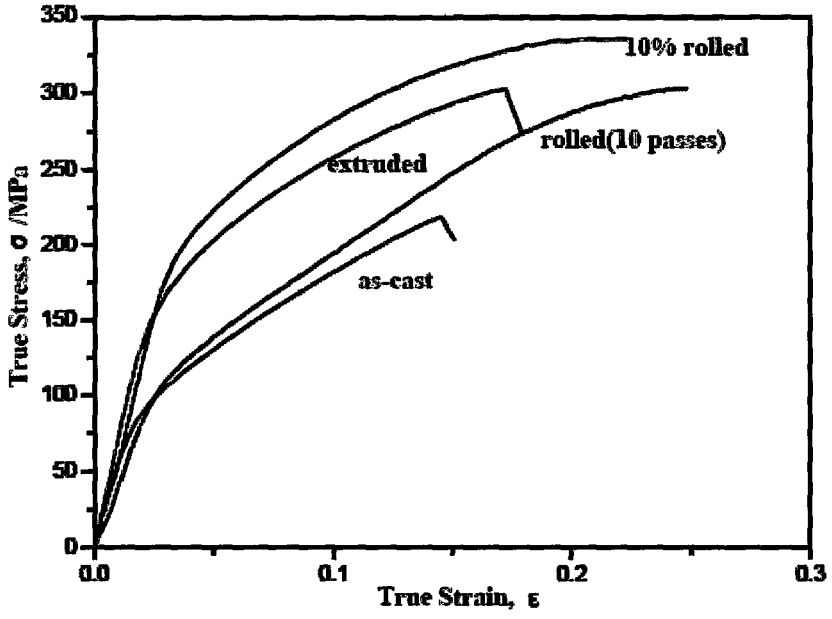

Figure 2.19 Flow curves for as-cast, extruded, and hot rolled AZ31 (Song et al. (2003)).

Bang et al. (2006) compared rolled and extruded AZ31 sheet at elevated temperatures. The elongation data at several temperatures is shown in Figure 2.20. At all temperatures, the rolled material was more ductile than the extruded. This difference increased as the test temperature was increased. This superior elongation was credited as the reason that the rolled material performed better in square cup drawing and press stamping tests. No attempt was made to isolate the grain size or texture effects in either of these studies, making definite conclusions as to why one material was better than another difficult.

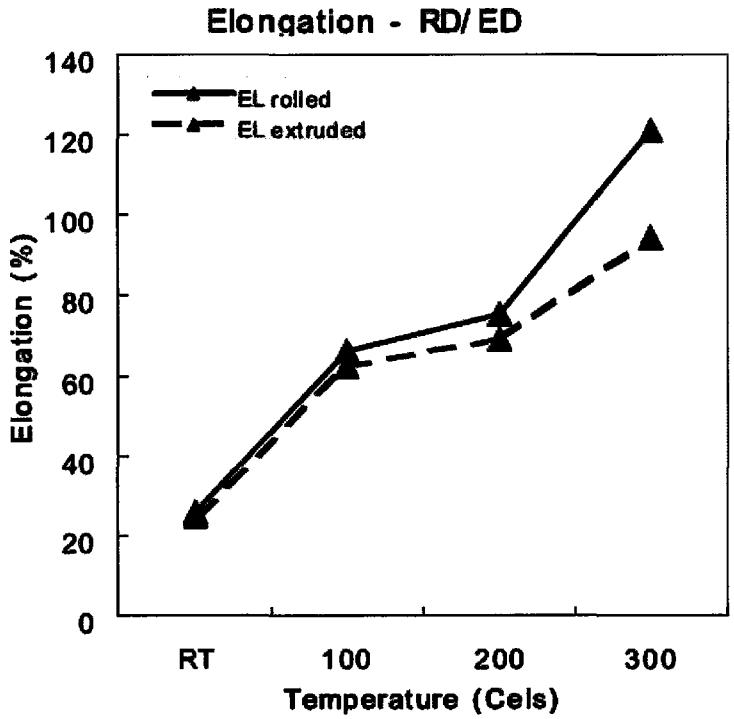

Figure 2.20 Elongation data for rolled and extruded AZ31 at several temperatures (Bang et al. (2006)).

3. Research Objectives

The objectives of this work are as follows:

1. Attempt to determine what microstructural factors cause the difference in formability between rolled and extruded magnesium sheet alloys.
2. Analyze the role of dynamic recrystallization on the flow properties of magnesium.
3. Use digital image correlation (DIC) to examine strain heterogeneities in magnesium, and to determine if magnesium alloys satisfy Considère's criterion prior to failure.

4. Experimental Procedures

4.1 Introduction

Two materials were used in this study: one conventionally rolled and one extruded magnesium AZ31 alloy. AZ31 was chosen for this study because it is the most commonly used wrought magnesium alloy. Each material was produced industrially.

The mechanical properties of each material must be investigated in any formability study. Tensile testing was performed to determine the flow properties and strain distribution of each material. The yield strength determines how much force is required to deform the material. Ductility is a measure of the ability of a material to flow plastically. Strain distribution measurements were taken to analyze any local strain that occurred during testing.

Microstructures were characterized by metallography and x-ray diffraction (XRD). Metallography was used to measure grain size and grain size distribution. Texture was measured through XRD.

4.2 Materials

Two wrought AZ31 sheet materials were used in this study: one conventionally rolled (designated R7) and one extruded (E). Both materials were produced commercially and supplied to McMaster by GM Corporate R&D Centre in Warren, MI. Material E was

extruded at 400°C, and was provided in the as-extruded state. R7, with the ASTM designation AZ31B-H24, was strain hardened, then partially annealed to become only "half hard". To achieve a 12 μm grain size in the rolled material, R7 was annealed for 8 hours at 400°C. The rolled material was received in sheet 2 mm thick, while E had a thickness of 1.65 mm. The chemical compositions, as determined by inductively coupled plasma spectrometry, are listed in Table 4.1. The data in this table is given in weight percent. The primary alloying elements in AZ31 are aluminum, zinc, and manganese. The aluminum and zinc amounts were very similar, while there was a slight variation in the amount of manganese. Overall, the chemistry differences were not believed to be significant.

Table 4.1 Chemical composition of the AZ31 sheets

	Al	Zn	Mn	Zr	Fe	Cu	Ni	Ca	Sr	Ce
R7	3.057	0.991	0.415	0.002	0.011	0.010	0.003	0.003	0.005	0.005
E	3.026	0.967	0.313	0.002	0.010	0.003	0.001	0	0	0.006

4.3 Tensile Testing

Uniaxial tensile tests were performed on an MTS servohydraulic test machine with a 5 kN load cell. Flat tensile specimens were prepared according to ASTM E-2448. The gauge section was 6 mm wide and 25 mm long. The samples had a fillet radius of 3 mm, which was 1.5 mm larger than the standard. The grip section was 25×15 mm. Samples were conventionally machined, and then stress-relieved at 345°C for 15 minutes.

All samples were tested such that the stress axis was parallel to the rolling or extrusion direction. Tests were performed at room temperature at a strain rate of 6.67×10^{-4}/s and at 200°C at strain rates of 6.67×10^{-4}/s and 6.67×10^{-3}/s. An Instron furnace was used for elevated temperature testing. This furnace was equipped with a low refractive index window, which allowed the sample to be observed during deformation. Room temperature tests with and without this window indicated that there were no significant differences in recorded strain. Samples were held at temperature for 10 minutes prior to testing. Two samples were tested for each condition. Strain measurements were taken using a commercially available digital image correlation (DIC) system (ARAMIS), which is discussed in detail below. This system outputs true strain, as it measures the instantaneous length of the sample. True stress was calculated from the recorded load data. Stress-strain curves were developed by correlating the frequency of recorded ARAMIS data to the frequency of load-displacement data recorded by the MTS software.

For analysis, the flow curves were fit to a model, such as the Holloman equation. Strain hardening rates were obtained from the derivative of the model, as opposed to the derivative of the experimental data. This was done so that a smooth curve was generated, so the point of intersection between the flow curve and strain hardening rate could be more accurately determined.

4.4 Digital Image Correlation

Digital image correlation (DIC) is a non-contact strain measurement method. A black and white random speckle pattern is applied to the surface of interest. A camera records pictures of this surface after an increment of deformation. The distribution of grey scale values in a small rectangular area called a facet is then calculated before and after each increment of deformation. Many facets make up the total area of interest. A reference point is defined in the original image, and must then be found in the deformed image. This process is depicted in Figure 4.1. The relationship between these points is represented by equation 4-1:

$$g_1(x,y) = g_2(x_t,y_t) \tag{4.1}$$

where g_1 and g_2 are the initial and deformed images, and x and y are the co-ordinates on the image. The pixels in each facet of the initial image are transformed onto the deformed image according to:

$$x_t = a_1 + a_2x + a_3y + a_4xy \tag{4.2}$$

$$y_t = a_5 + a_6x + a_7y + a_8xy \tag{4.3}$$

where a_1 and a_5 describe the translation of the facet centre, and a_2-a_4 and a_6-a_8 describe the rotation and deformation of the facet. A linear radiometric transformation is used to compensate for differences in brightness between the initial and deformed image:

$$g_1(x,y) = b_1 + b_2g_2(x_t,y_t) \tag{4.4}$$

The parameters a_1-a_8 and b_1-b_2 are calculated to minimize the sum of the quadratic deviation of the matched grey scale values (Aramis (2001)).

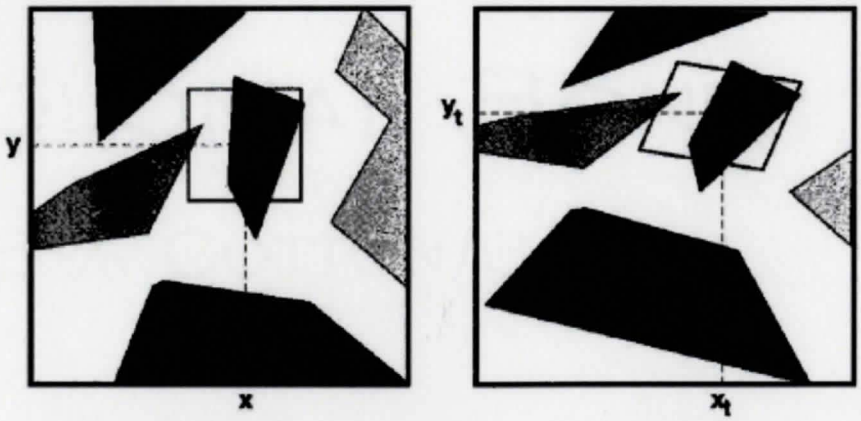

Figure 4.1 Principle of digital image correlation showing initial and deformed images (Aramis 2001).

DIC has been used to measure local strains in aluminum (Kang et al. (2005)), strain heterogeneities in epoxy resin reinforced with glass fibers (Godara and Raabe (2007)), strain distribution in dual phase steels (Kang et al. (2007)) and true stress-strain curves beyond diffuse necking in AZ31 (Marya et al. (2006)). Tensile testing has been performed up to 650°C, but only to strains of 0.02 (Lyons et al. (1996)).

In this study, black high temperature spray paint was used to apply a random speckle pattern to the surface of the tensile specimens. The natural gray colour of the magnesium samples provided good contrast with the black paint. The images were recorded using an LCD camera. Images were recorded every 0.5 second during room temperature tests and 200°C tests at a strain rate of 6.67×10^{-3}/s. This image acquisition rate represented the upper limit of the camera. Images were recorded every four seconds for tests at 200°C at a strain rate of 6.67×10^{-4}/s. This image acquisition rate was

considered to be optimal for these test conditions. ARAMIS can only process 500 images per test, so this rate allowed the entire test to be recorded and processed.

A facet size of 11×13 pixels along with a facet step of 9 pixels was used. The facet step refers to the distance between the left edge of one facet to the left edge of the adjacent facet. Prior to strain measurement, the images were calibrated using the width of the sample's gauge section (6 mm). The stability of the center of each facet from stage to stage was the limiting factor in determining the accuracy of ARAMIS data. This point can only move 0.04 pixels. With a field of view of 186 mm (length of tensile samples on a recorded image) and a screen resolution of 1280×1024 pixels, the maximum error in a measurement was 6.2 μm. True strain data and strain contour maps were obtained directly from ARAMIS.

4.5 Microstructure Characterization

Standard techniques were used to observe the microstructure of the magnesium samples. Each sample was cold mounted in epoxy resin. They were ground with 800 and 1200 grit silicon carbide papers, and then polished with 9 μm and 3 μm oil-based diamond suspensions. The final step was a 0.05 μm Al_2O_3 powder suspended in an 80/20 ethanol/glycerine mixture. Acetic-picral was the etchant used. Metallography was performed on samples in the stress-relieved condition, so that the material's

microstructure immediately before tensile testing could be examined. Microstructures after tensile testing were also examined.

Grain size was measured using the linear intercept method. Four lines with random orientations were drawn on each image. At least 20 grains intersected each line. The average number of grains per line was then calculated.

Texture measurements were performed using a Bruker X-ray diffraction goniometer along the rolling direction using Cu Kα radiation. MTM-FHM software was used to generate (0002) pole figures and to analyze the fraction of grains oriented close to the basal plane. Equation 4.5 was used for the volume fraction (V_f) calculations:

$$V_f = \frac{\int_0^{\beta_c}\int_0^{2\pi} I(\alpha,\beta)\sin(\beta)d\alpha \cdot d\beta}{\int_0^{\frac{\pi}{2}}\int_0^{2\pi} I(\alpha,\beta)\sin(\beta)d\alpha \cdot d\beta} \tag{4.5}$$

where I is the peak intensity, α and β describe the diffraction vector, and β_c is the angle from the pole of interest. Figure 4.2 illustrates this. Thus, the intensity around a ring a certain angle (β_c) away from the basal plane was divided by the intensity of the entire (0002) pole figure.

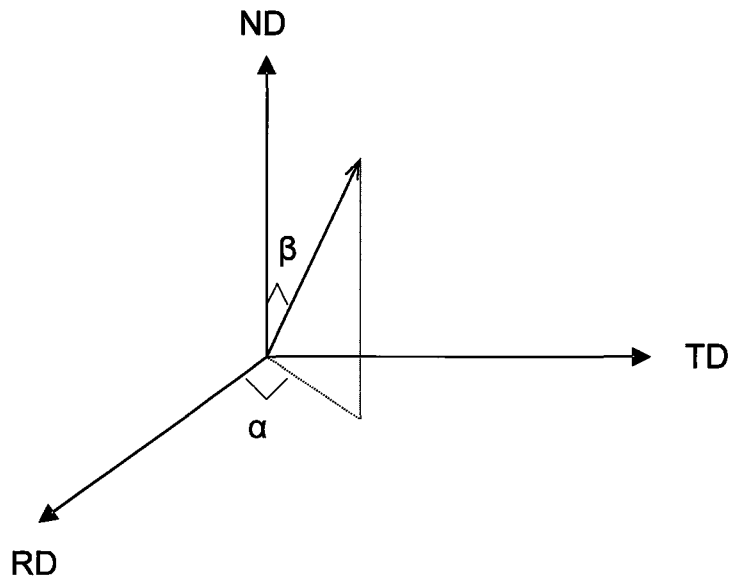

Figure 4.2 Geometry behind x-ray diffraction volume fraction calculations.

The fraction of recrystallized grains was measured by constructing a rectangular grid on the original metallographic image. The percent of recrystallized grains in each grid section was then estimated manually. The estimates from each grid section were then averaged to give an overall estimate of percent recrystallized. The strain at which these measurements were taken was calculated from the instantaneous width of the deformed tensile sample.

4.6 Fracture Surface Analysis

Fracture surface analysis was performed to determine the failure mechanisms of each alloy. A Phillips 715 scanning electron microscope (SEM) was used. The accelerating voltage was 20 kV, and the beam current was 20 μA. Images were recorded

at several magnifications. These images were also used to calculate the true fracture strain (ε_f) of the samples tested at 200°C. Equation 4.6 was used for these calculations:

$$\varepsilon_f = \ln \frac{A_0}{A_f} \tag{4.6}$$

where A_0 and A_f are the original cross-sectional area and the area after fracture. A Bridgmann correction factor C was used to account for stress triaxiality in the neck zone for the fracture stress (σ_f) calculations:

$$\sigma_f = C\frac{F_f}{A_f} = \frac{\sqrt{3}F_f}{2\left(1+\frac{t_f}{6R}\right)A_f} \tag{4.7}$$

where F_f is the load at fracture, tf is the sample's thickness at fracture, and R is the radius at the fracture point (Vazhentsev and Isaev, 1988).

5. Results

This chapter contains the experimental results of this research. The microstructures of each material were characterized via optical microscopy and XRD. Flow properties were analyzed by tensile testing. The deformed microstructures and fracture surfaces were examined. Strain distribution was measured via DIC, and compared against Considère's criterion.

5.1 Initial Microstructure

5.1.1 Optical Microscopy

The starting microstructures of each alloy are presented in Figures 5.1 and 5.2. The rolling direction is vertical. In both materials, the grains were round and equiaxed. R7 had a grain size of 7 μm, while E had a grain size of 12 μm. Each grain size distribution was unimodal. Second phase particles were observed in unetched samples shown in Figure 5.2. These contained Al and Mn. No differences in the size or shape of these particles were observed between the two alloys.

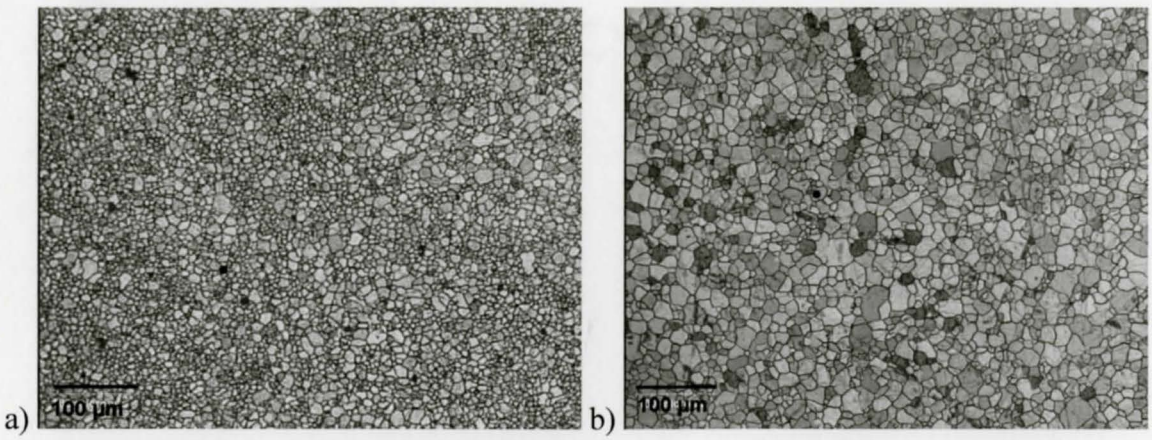

Figure 5.1 Etched optical micrographs of a) R7 and b) E. The micron marker is 100 µm.

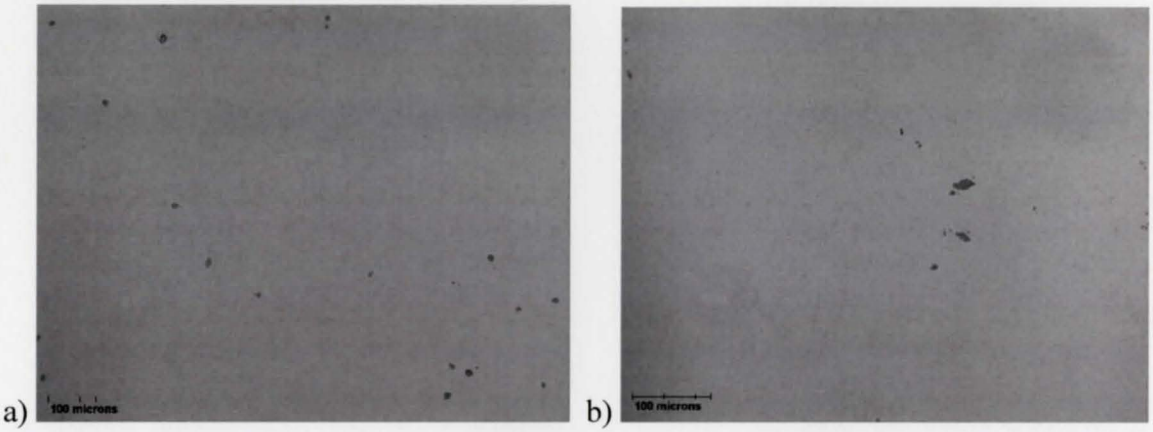

Figure 5.2 Unetched optical micrographs of a) R7 and b) E. The micron marker is 100 µm.

5.1.2 Texture

The starting texture of each material was characterized through x-ray diffraction. (0002) pole figures are shown in Figures 5.3 and 5.4. The rolling/extrusion direction is horizontal. These pole figures were indicative of the texture difference between the two materials. R7 had the typical wrought magnesium texture, with the basal plane parallel to the rolling direction. E had a basal texture that was slightly inclined from the extrusion

direction. The rolled material had a slightly more random texture, with a maximum contour of 8 times random, while that of E was 11 times random.

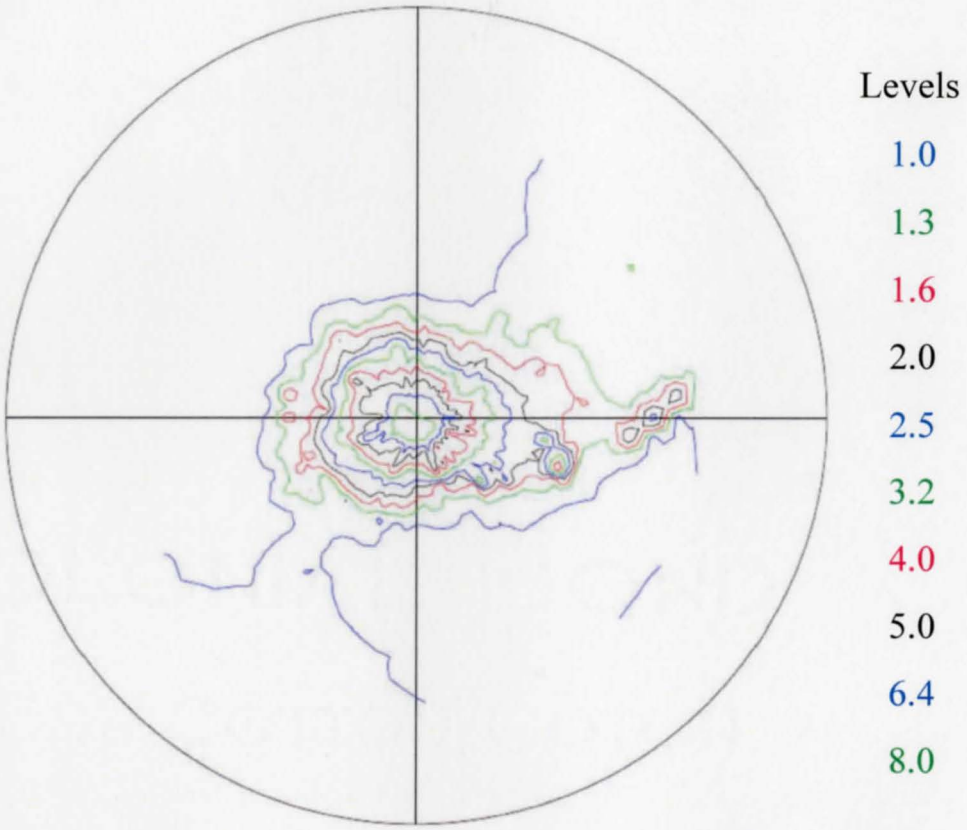

Figure 5.3 Initial (0002) pole figure for R7.

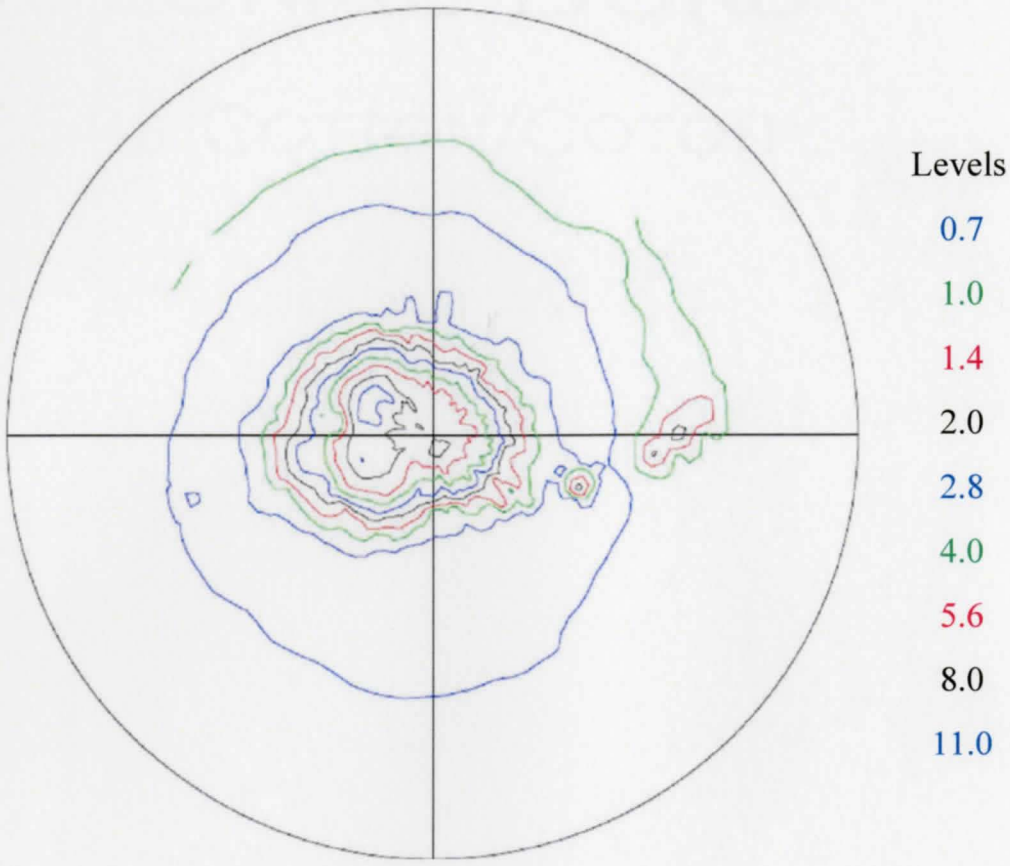

Figure 5.4 Initial (0002) pole figure for E.

5.2 Tensile Testing

Tensile tests were performed on both materials at room temperature and 200°C. The room temperature true stress-true strain data is shown in Figure 5.5, while the 200°C data is shown in Figures 5.6 and 5.7. These curves only show data until the point of maximum load. At room temperature, R7 had a higher 0.2% yield strength of 155 MPa, compared to 149 MPa for E. E had a larger strain hardening rate. R7 had a longer elongation of 17.1%, while that of E was 15.6%.

At 200°C and $6.67\times10^{-4}s^{-1}$, R7 had a yield strength of 78 MPa and an elongation of 66.9%, compared to 74 MPa and 51.2% for E. The true fracture strain for R7 was 4.75, which was larger than 1.13 for E. At $6.67\times10^{-3}s^{-1}$, R7 had a yield strength of 116 MPa with an elongation of 53.7% and a true fracture strain of 3.41. E had a yield strength of 105 MPa, an elongation of 44.0%, and a true fracture strain of 1.32. The extruded material had a higher strain hardening rate at both strain rates. At all temperatures, the smaller grained material (R7) had a higher yield strength and elongation to failure, which was consistent with the literature. Materials tested at 200°C had longer elongations and lower yield strengths than room temperature tests, as expected.

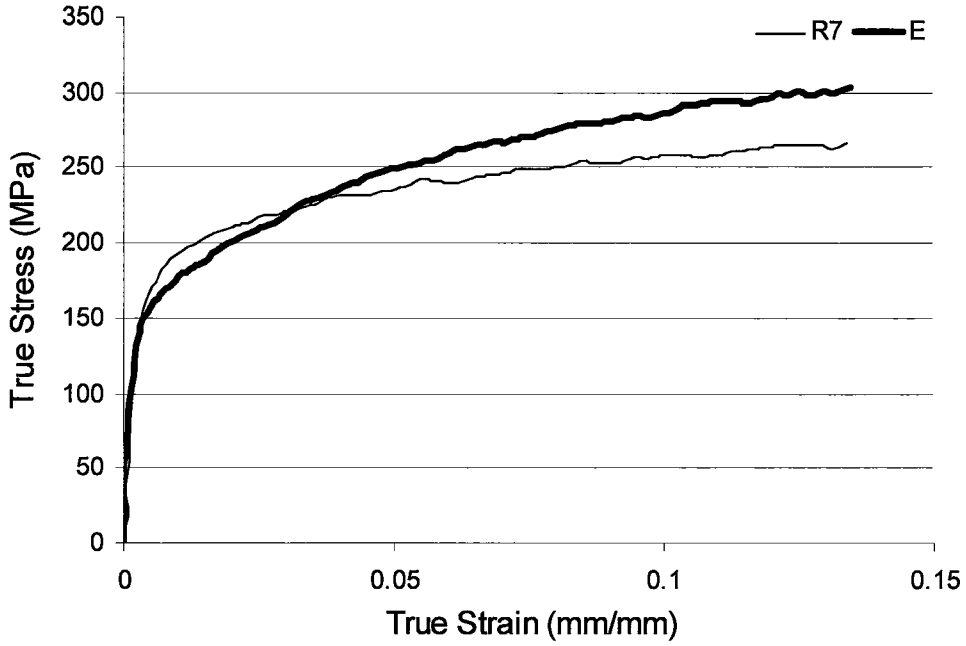

Figure 5.5 Room temperature stress-strain curve at $6.67\times10^{-4}s^{-1}$.

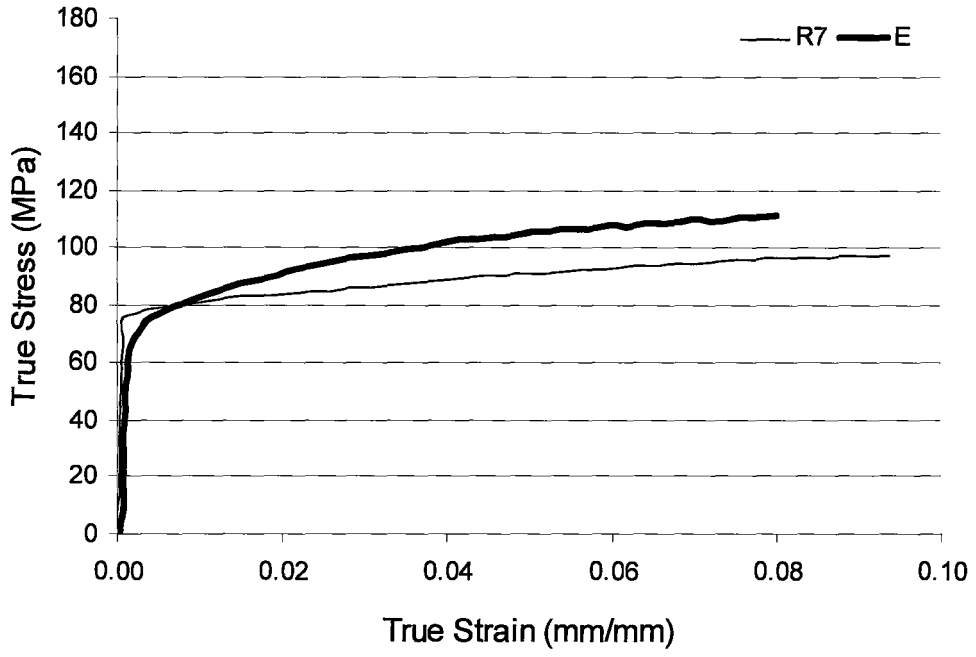

Figure 5.6 200°C stress-strain curve at $6.67\times10^{-4}s^{-1}$.

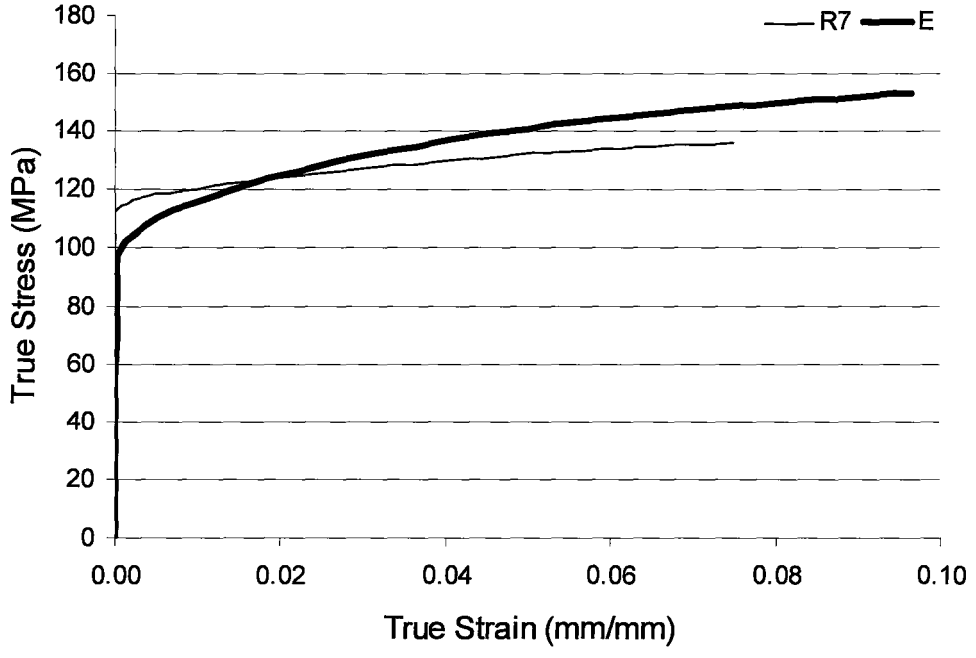

Figure 5.7 200°C stress-strain curve at $6.67\times10^{-3}s^{-1}$.

Room temperature and 200°C $6.67\times10^{-3}s^{-1}$ data were fit to standard equations to calculate the strain hardening rate and instability strain. The results are shown in Table 5.1 and Figures 5.8 and 5.9, along with the global strain at which instability occurred (ε_{glo}) and the theoretical instability strain (ε_{theo}). Figures 5.10 to 5.13 plot the modeled flow curves against the strain hardening rate. In all four cases, the material softened before the strain hardening rate intersected the flow curve. The instability condition was not satisfied. Both R7 and E softened at similar strains. However, E had a much higher strain hardening rate, meaning that its capacity for stable flow was higher. At 200°C, the difference between ε_{theo} and ε_{glo} was 0.012 for R7 and 0.027 for E. The 12 μm grained material, with the higher strain hardening rate, had a longer stable flow region than the 7 μm material. Thus, the material with the higher strain hardening rate had better formability.

Table 5.1 Modeling parameters for instability condition.

Material	Temperature	Equation	K	n	σ_0	ε_{theo}	ε_{glo}	$\frac{d\sigma}{d\varepsilon}$ (MPa)
R7	RT	$\sigma = K\varepsilon^n$	455	0.163	-	0.163	0.133	356
E	RT	$\sigma = K\varepsilon^n$	491	0.218	-	0.218	0.135	492
R7	200°C	$\sigma = \sigma_0 + K\varepsilon^n$	80	0.360	105	0.087	0.075	150
E	200°C	$\sigma = K\varepsilon^n$	205	0.123	-	0.123	0.096	195

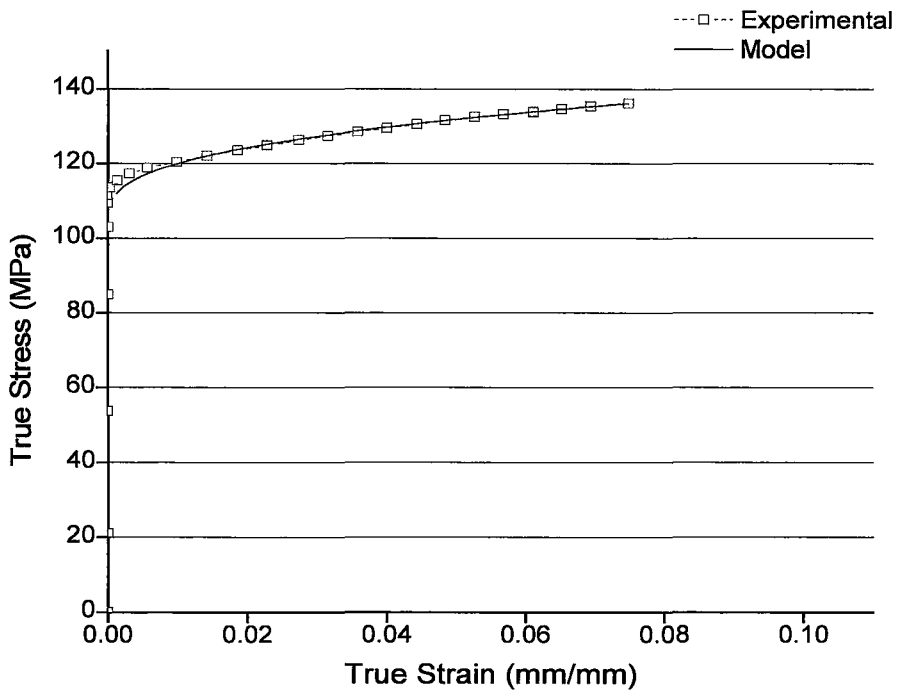

Figure 5.8 Experimental data and standard equation fit for R7 at 200°C $6.67\times10^{-3}s^{-1}$.

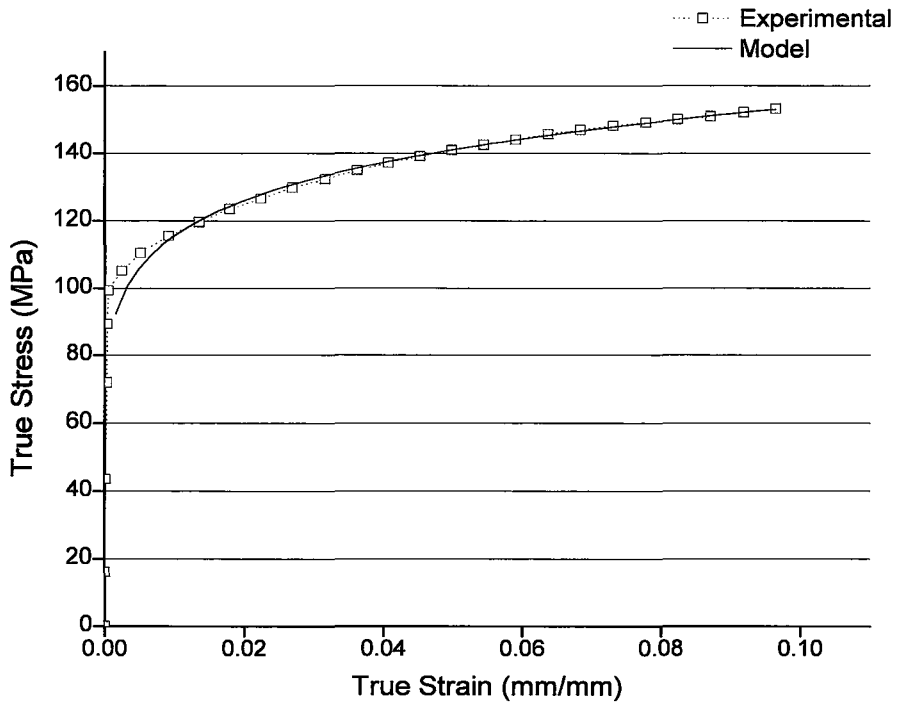

Figure 5.9 Experimental data and standard equation fit for E at 200°C $6.67\times10^{-3}s^{-1}$.

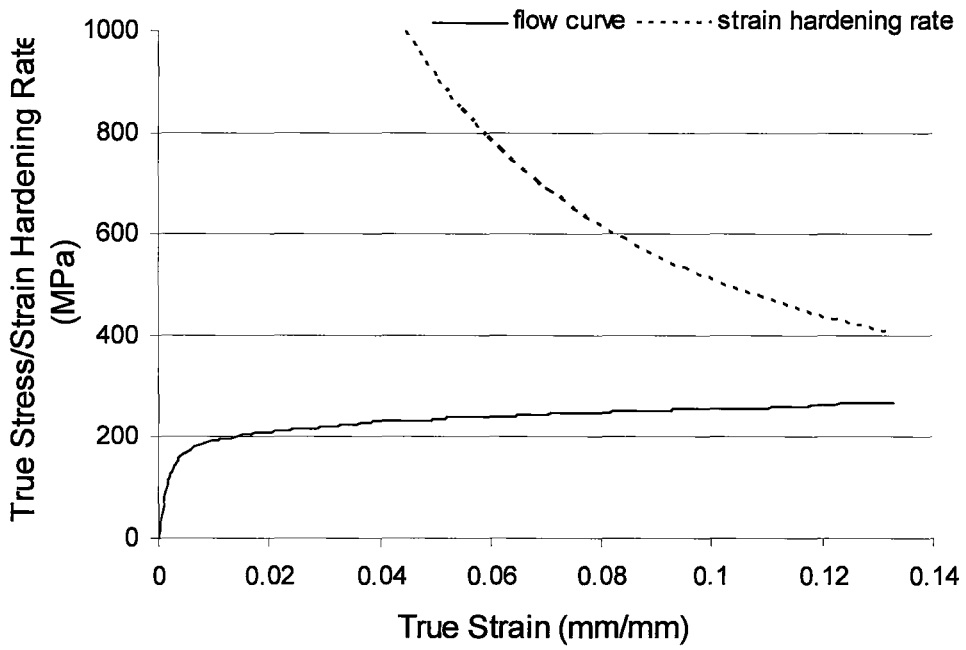

Figure 5.10 Strain hardening rate and true stress for R7 at RT $6.67\times10^{-4}s^{-1}$.

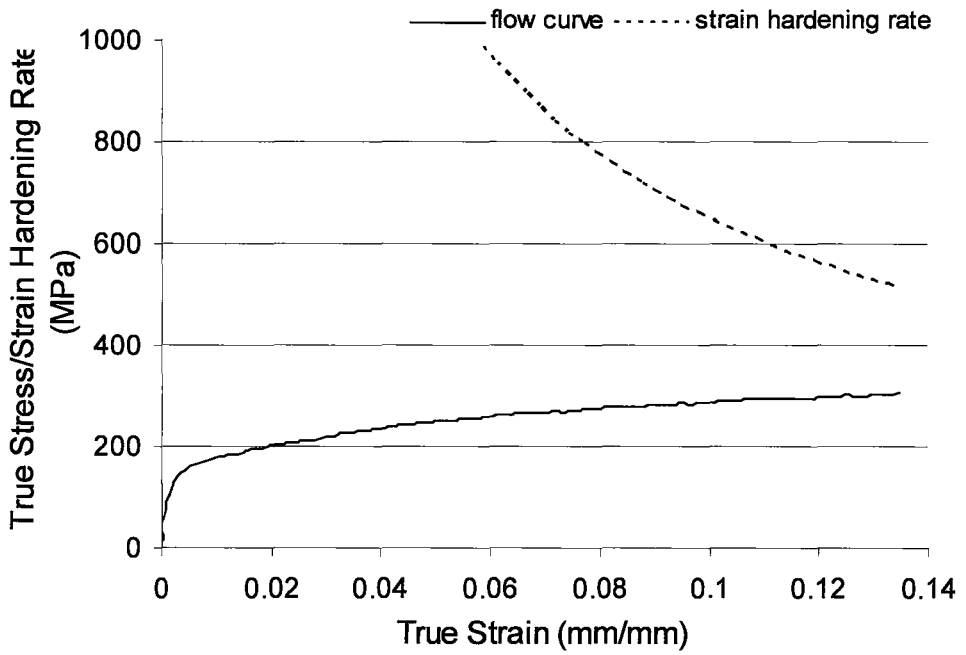

Figure 5.11 Strain hardening rate and true stress for E at RT $6.67\times10^{-4}s^{-1}$.

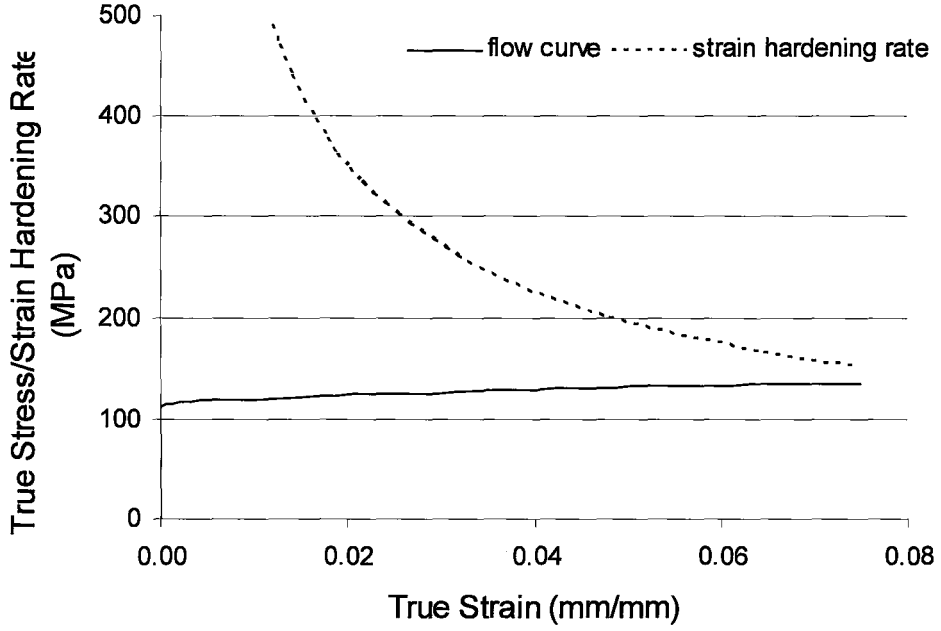

Figure 5.12 Strain hardening rate and true stress for R7 at 200°C $6.67\times10^{-3}s^{-1}$.

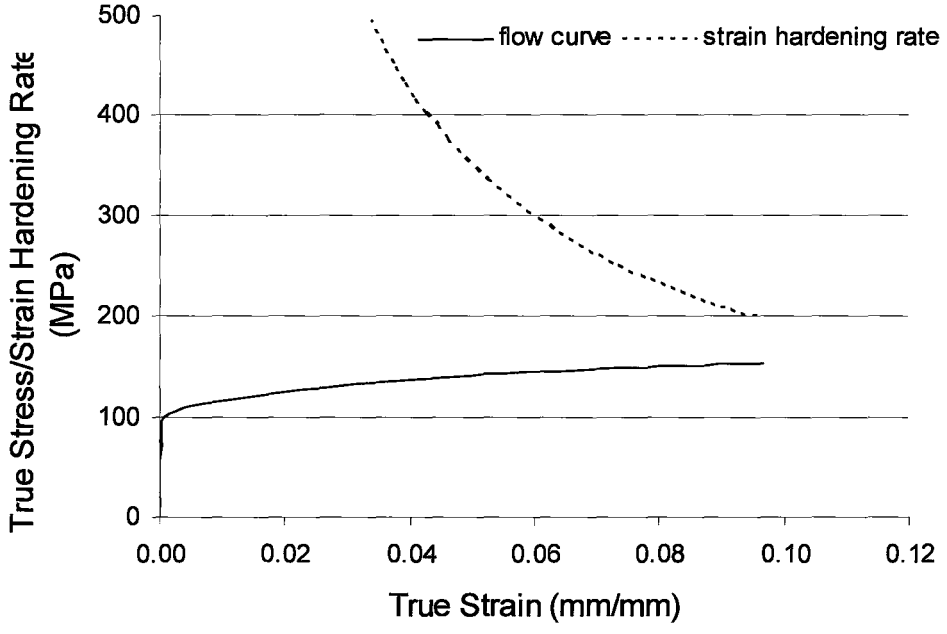

Figure 5.13 Strain hardening rate and true stress for E at 200°C $6.67\times10^{-3}s^{-1}$.

5.3 Eliminating Grain Size Effect

To eliminate the effects of grain size, R7 was annealed to increase the grain size to 12 μm. This material was designated R12. Figures 5.14 and 5.15 show the initial microstructure and texture of this material. Again, the grains were equiaxed, and the distribution was unimodal. The texture of R12 was similar to that of R7. Tensile tests on this material were performed at 200°C $6.67\times10^{-4}s^{-1}$ Figure 5.16 compares these results to those of R7 and E. R12 had a lower yield strength (66 MPa) than R7, likely due to its larger grain size. The true fracture strain for this material was 4.38, which was slightly less than R7, but much higher than E at the same grain size. The elongation was 65.6%, which was very close to R7 (66.9%). The strain hardening exponent for R12 was 0.150.

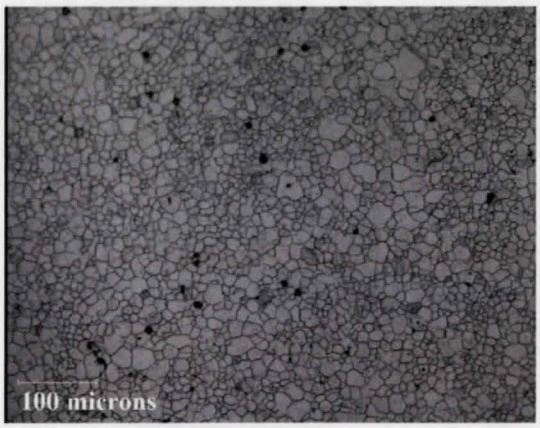

Figure 5.14 Optical micrograph of R12, showing equiaxed grains and unimodal distribution.

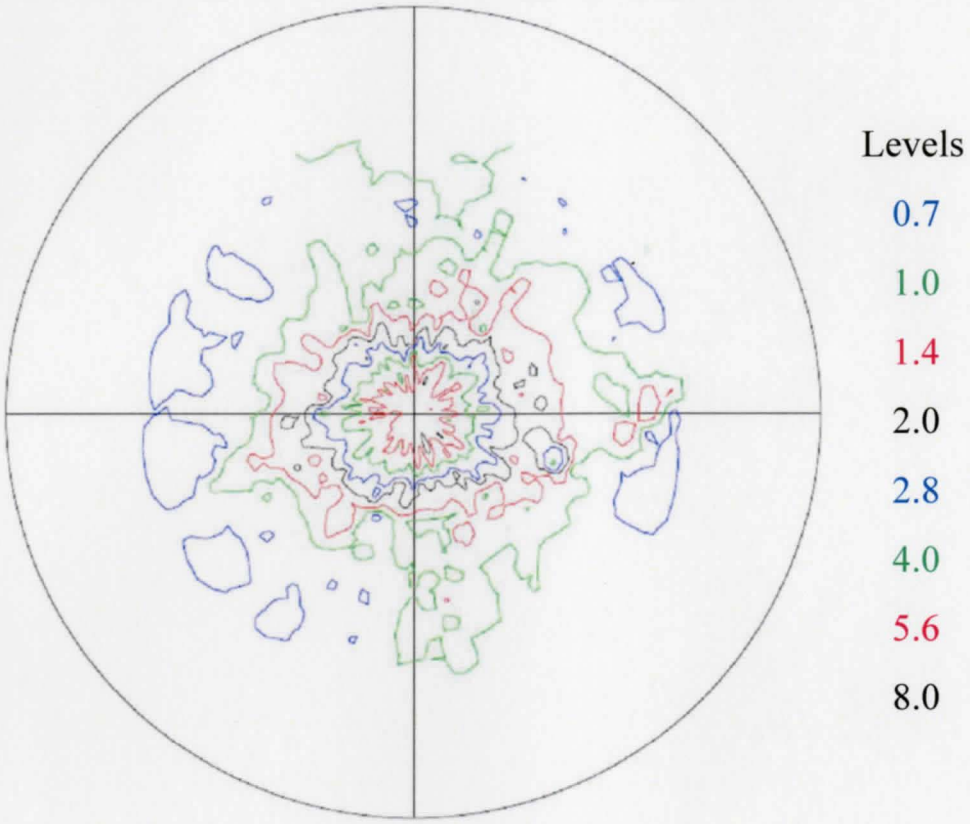

Figure 5.15 Initial (0002) pole figure for R12.

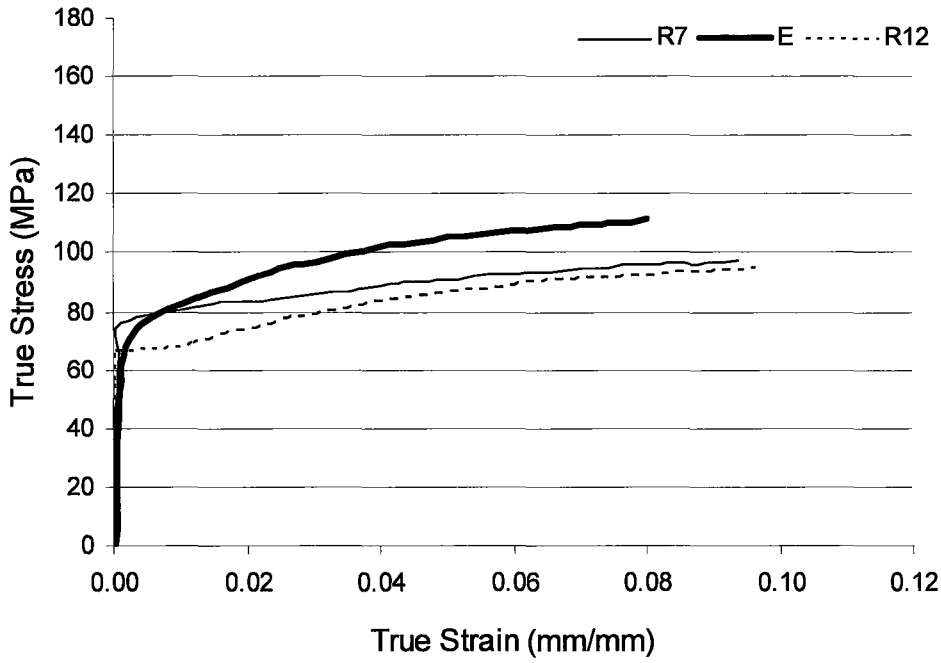

Figure 5.16 Flow curves of R7, R12, and E at 200°C $6.67\times10^{-4}s^{-1}$.

These true stress-true strain curves were extended to fracture by estimating the instantaneous cross-sectional area at various points during testing. This can be accomplished since ARAMIS records images continuously during a test. Therefore, a sample's width can be measured at these points. The sample's thickness was estimated from *r*-values that were measured from deformed samples after testing. The tensile load was determined by relating the ARAMIS image (each image recorded during a test was number sequentially) to load data outputted by the MTS software. True fracture strain was calculated by measuring the cross-sectional area of the fracture surface (via SEM images). The load at fracture was then used to calculate the true fracture stress. Thus, true stress at any step can be estimated. Figure 5.17 shows the flow curves that were

generated. A two-stage flow curve was observed in R7 and R12. These materials strain hardened initially, and then softened considerably prior to fracture. However, the extruded material showed initial work hardening to a plateau stress, followed by limited softening until fracture.

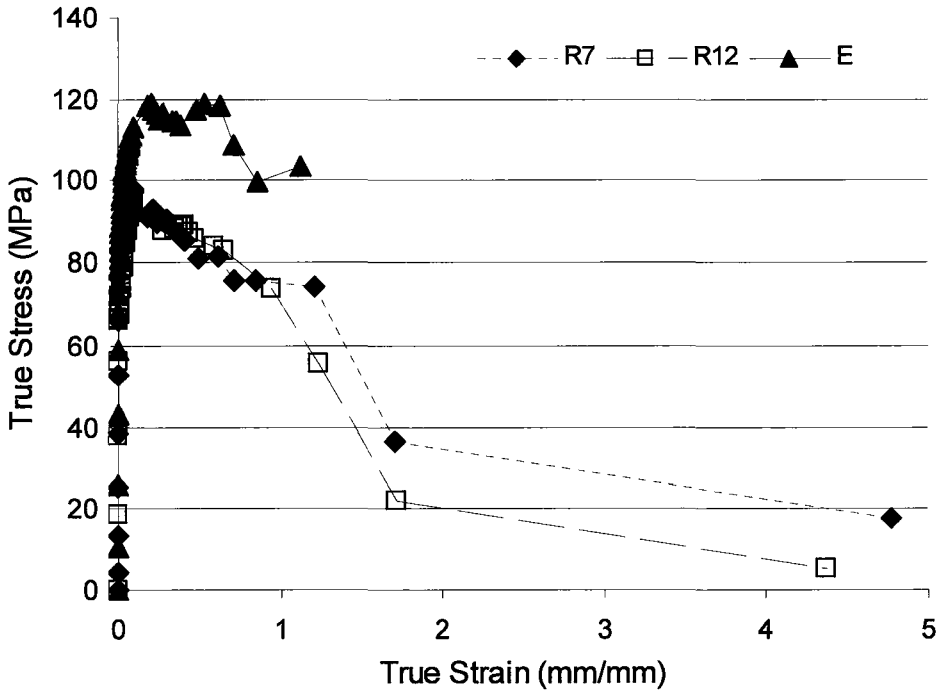

Figure 5.17 True stress-strain curves to fracture produced by estimating the instantaneous cross-sectional area. The data was taken from tests at 200°C $6.67\times10^{-4}s^{-1}$.

5.4 Deformed Microstructure

The fillet sections of the tensile coupons were examined after tensile testing to observe the microstructure. Figures 5.18 shows the microstructures of the room temperature samples at the fracture point. Extensive twinning was observed in both of the room temperature samples at fracture. Figures 5.19 to 5.24 show the microstructures for

R7, R12, and E at several strains following deformation at 200°C $6.67\times10^{-4}s^{-1}$ No twinning was observed at this higher temperature. Dynamic recrystallization (DRX) was prevalent. Nucleation of the new grains initiated at grain boundaries. The fraction of new grains was higher in R7 than in R12 or E, indicating that the smaller grain size promoted nucleation of new grains. Necklace type recrystallization was observed in E.

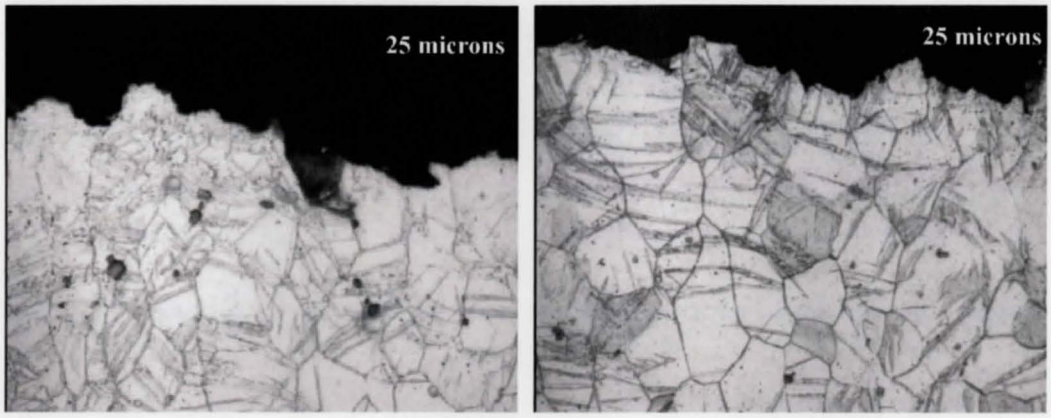

Figure 5.18 Microstructure at fracture for R7 and E, respectively Tested at room temperature $6.67\times10^{-4}s^{-1}$

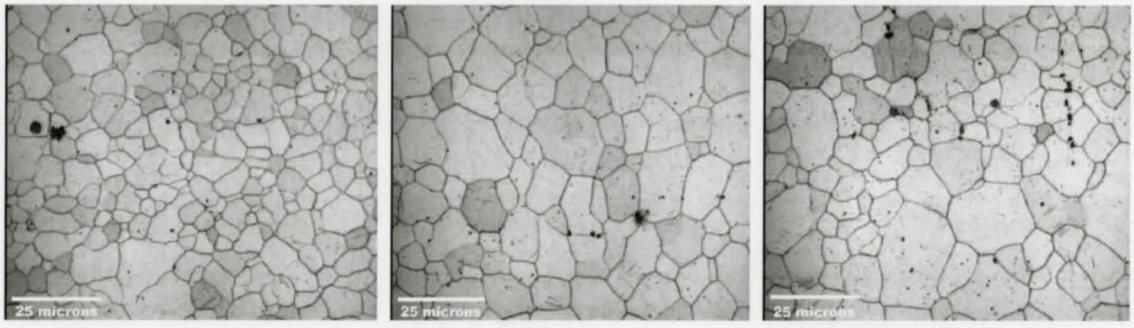

Figure 5.19 Starting microstructures of R7, R12, and E, respectively

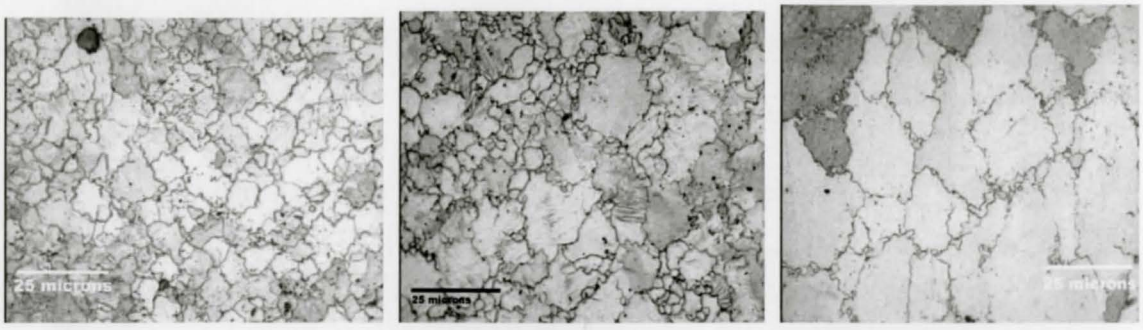

Figure 5.20 Deformed microstructure at a strain of 0.15 for R7, R12, and E, respectively. Tested at 200°C $6.67\times10^{-4}s^{-1}$.

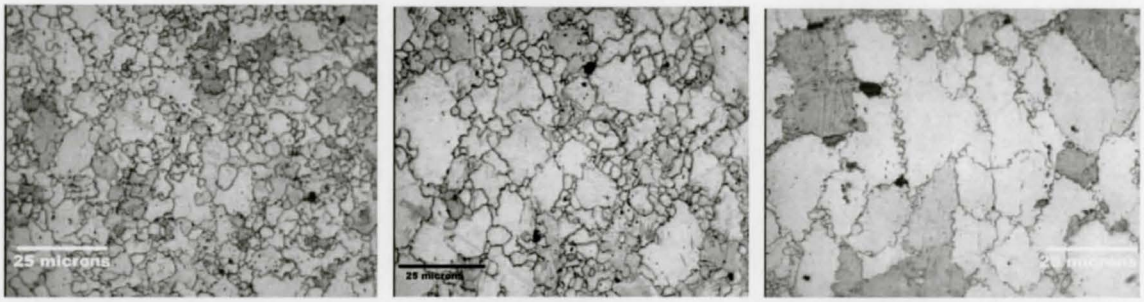

Figure 5.21 Deformed microstructure at a strain of 0.20 for R7, R12, and E, respectively Tested at 200°C $6.67\times10^{-4}s^{-1}$.

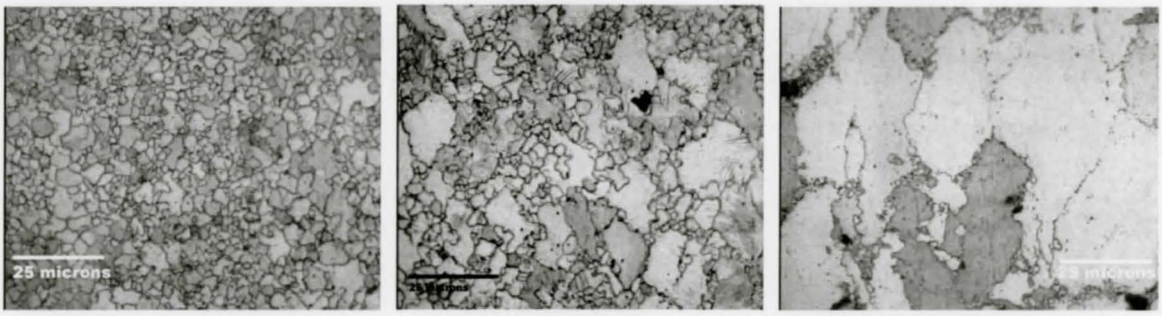

Figure 5.22 Deformed microstructure at a strain of 0.25 for R7, R12, and E, respectively. Tested at 200°C $6.67\times10^{-4}s^{-1}$.

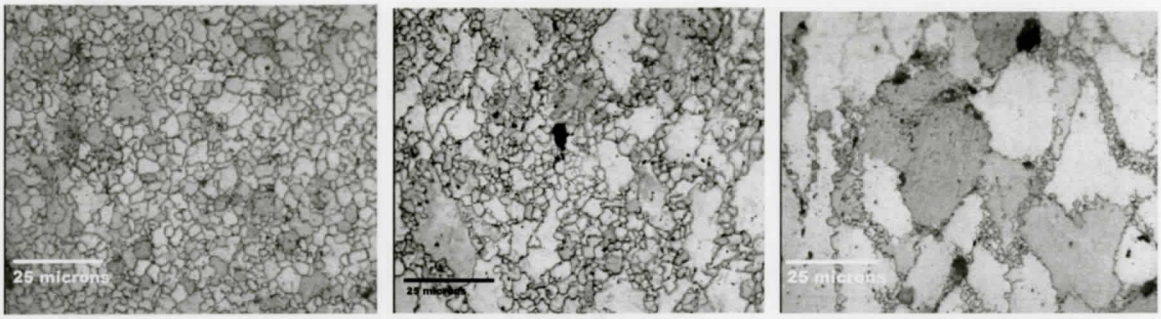

Figure 5.23 Deformed microstructure at a strain of 0.30 for R7, R12, and E, respectively. Tested at 200°C $6.67\times10^{-4}s^{-1}$

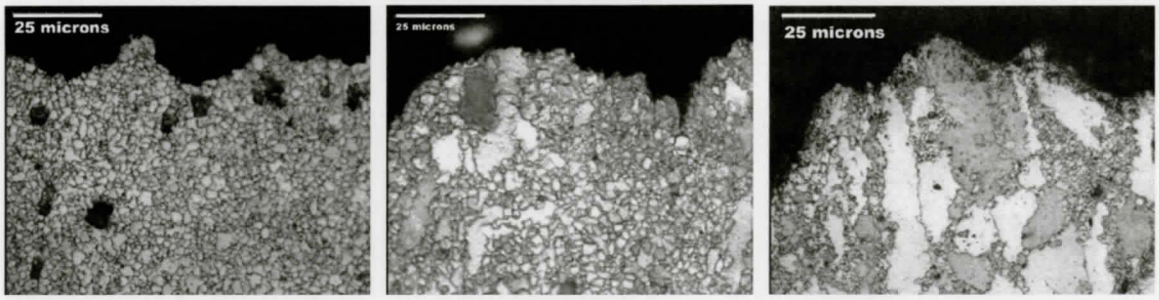

Figure 5.24 Deformed microstructure at fracture for R7, R12, and E, respectively Tested at 200°C $6.67\times10^{-4}s^{-1}$

5.5 DIC Strain Mapping

The strain distribution at the tensile instability point was examined using DIC. The results are shown in Figures 5.25 to 5.28. Note that what is pictured is the component of strain along the tensile axis, ε_y. These figures are overlays of the gauge section of tensile specimens. A strain scale is pictured beside each image. Strain heterogeneities, or 'hot spots', were present in all four instances. The peak strain is labeled in each figure. The 'hot spots' observed at the edges of some specimens (Figures 5.25 and 5.27) were believed to be due to calculation errors, and do not represent real regions of strain

localization. These peak strain localization values were compared to the theoretical and globally measured instability strains in Table 5.2. Under all four test conditions, the local strain measured through DIC was within 5% of the theoretical instability strain calculated from the fitted equations.

This relationship could only be measured and compared with theoretical data at room temperature and at 200°C $6.67\times10^{-3}s^{-1}$ An image acquisition rate of two images per second was possible for these tests. At 200°C $6.67\times10^{-4}s^{-1}$, ARAMIS images could only be recorded every four seconds. With this lower temporal resolution, it was believed that local strains causing instability were simply missed by the software.

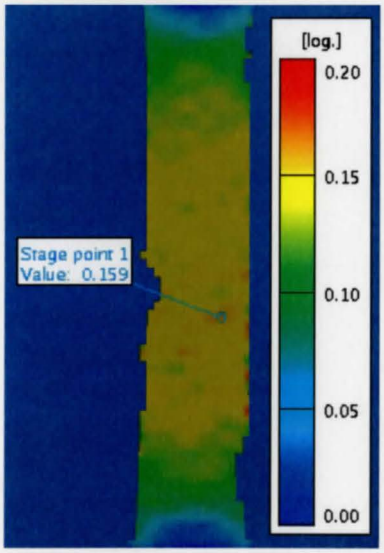

Figure 5.25 Room temperature strain distribution in R7 at instability point calculated through DIC. The largest strain value is 0.159.

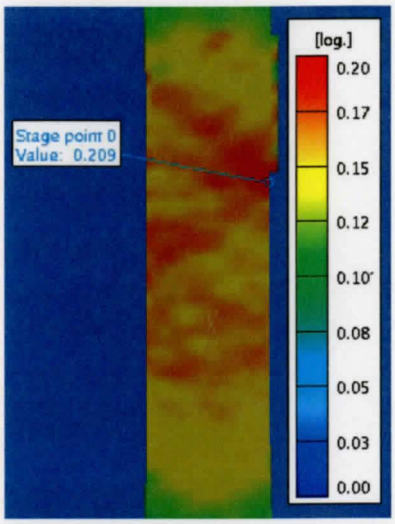

Figure 5.26 Room temperature strain distribution in E at instability point calculated through DIC. The largest strain value is 0.209.

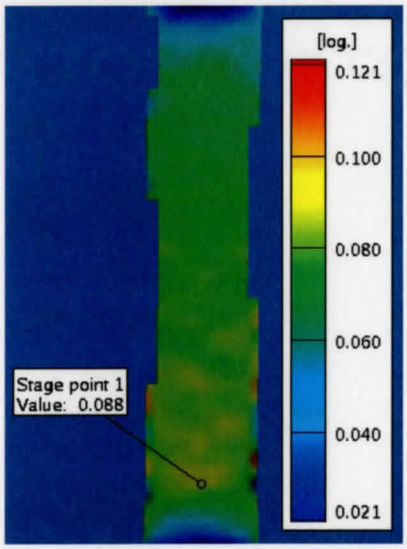

Figure 5.27 200°C $6.67\times10^{-3}s^{-1}$ strain distribution in R7 at instability point calculated through DIC. The largest strain value is 0.088.

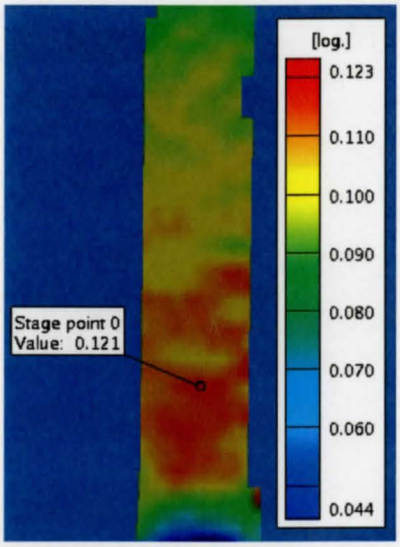

Figure 5.28 200°C $6.67\times10^{-3}s^{-1}$ strain distribution in E at instability point calculated through DIC. The largest strain value is 0.121.

Table 5.2 Theoretical, global, and local strains at the instability point.

Material	Temperature	ε_{theo}	ε_{glo}	ε_{local}
R7	RT	0.163	0.133	0.159
E	RT	0.218	0.135	0.209
R7	200°C	0.087	0.075	0.088
E	200°C	0.123	0.096	0.121

Figures 5.29 and 5.30 show true strain (ε_y) profiles along the gauge length of tensile specimens at room temperature for R7 and E. The lines on the graphs represent strain data for every tenth stage. One stage is one image recorded from the DIC camera, which corresponded to a strain of approximately 0.001 per image. The strain fluctuated about some mean value for each strain increment. In most cases, local strain peaks initiated early in the test, and persisted until failure. For R7, these peaks can be seen at

1.5, 7, 10, 12, and 13 mm along the gauge length. Similar peaks were observed in E at distances of 3.5, 7, 9, 13.5, and 17 mm.

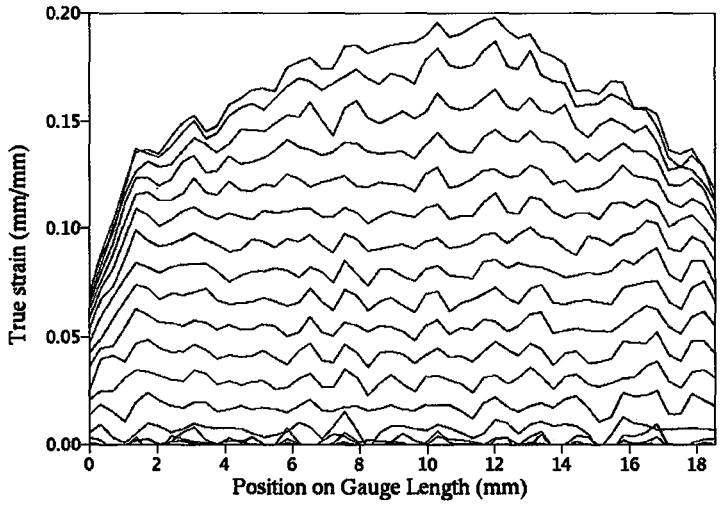

Figure 5.29 Strain profile along the gauge length for R7 at room temperature.

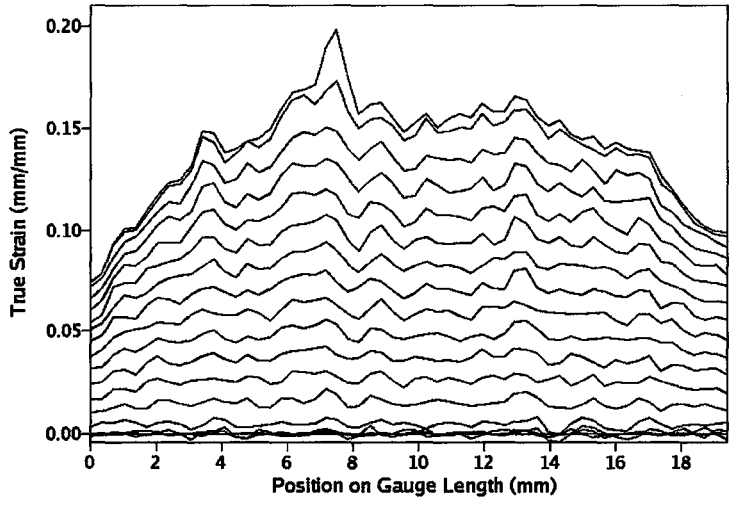

Figure 5.30 Strain profile along the gauge length for E at room temperature.

Similar data is shown for the 200°C tests in Figures 5.31-5.34. The extent of diffuse and localized necking was much more prevalent at 200°C than room temperature. The large peak in each of these graphs indicated localized necking. Deformation appeared to be uniform until strains of 0.2-0.25 were reached. Since this is above the Considère strain, it can be assumed that diffuse necking occurred in this strain range. Localized necking began at higher strains. Under both strain rates, R7 had a greater degree of localized necking. The lower strain rate resulted in larger strains.

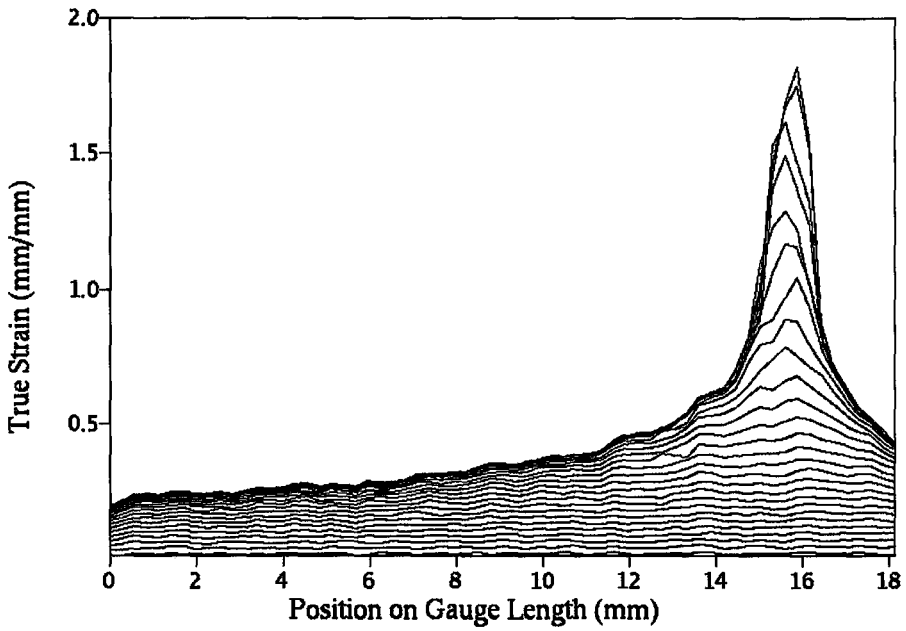

Figure 5.31 Strain profile along the gauge length for R7 at 200°C $6.67\times10^{-4}s^{-1}$.

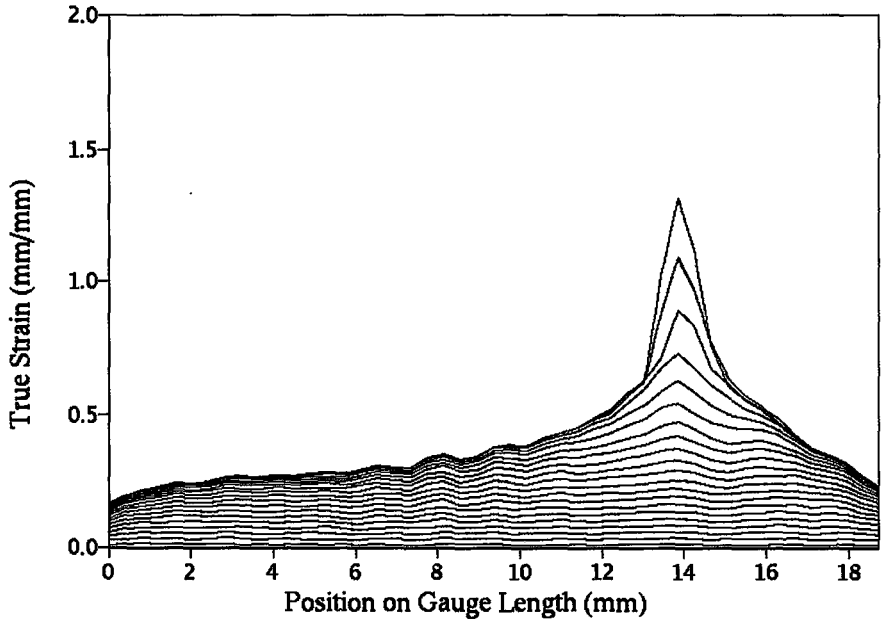

Figure 5.32 Strain profile along the gauge length for E at 200°C $6.67\times10^{-4}s^{-1}$.

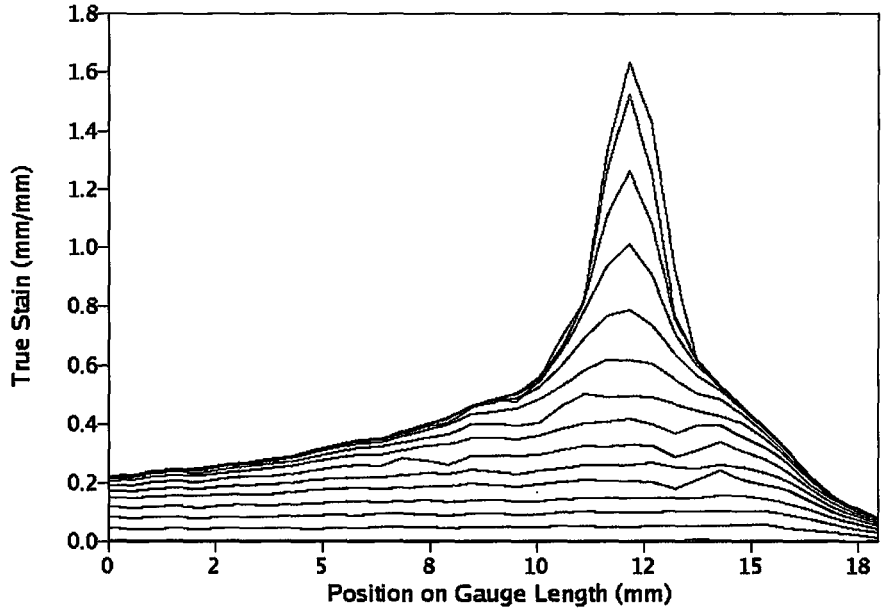

Figure 5.33 Strain profile along the gauge length for R7 at 200°C $6.67\times10^{-3}s^{-1}$.

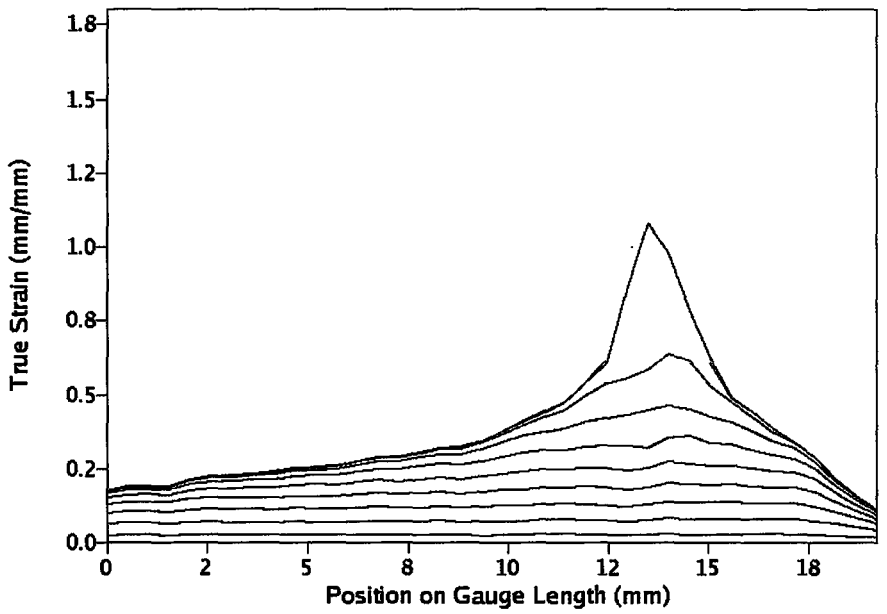

Figure 5.34 Strain profile along the gauge length for E at 200°C $6.67\times10^{-3}s^{-1}$.

Interrupted tensile tests were performed in an effort to determine what caused the strain localizations. A metallographic examination of tensile coupons stopped at strains of 0.002 and 0.01 showed no microstructural differences along the gauge length of the specimen. At room temperature, no evidence of localized twinning was found. Similarly, at 200°C, no evidence of localized regions with extensive DRX was observed. One possible explanation is that small regions of grains with orientations favourable for slip exist along the sample's gauge length. These regions would deform to a greater extent than the surrounding material.

5.6 Fracture Surface Analysis

Specimens tested at 200°C were subjected to fracture surface analysis using an SEM to examine the fracture behaviour. The images are displayed in Figures 5.35-5.37. Void coalescence was the dominant fracture mode in R7 and R12. Both these materials necked down to a thin section. In contrast, E exhibited a mixed mode of fracture. Void coalescence and transgranular shear fracture were observed. The two arrows in Figure 5.36 point to areas where void coalescence appeared to surround a larger transgranular fracture area. It was believed that the smaller, recrystallized grains promoted void coalescence, and the larger, retained grains in E failed via transgranular fracture. Void nucleation was observed at the fine-coarse grain interface in the optical micrographs of E in Figures 5.23 and 5.24. Voids were also observed near the fracture point in R7 and R12 in these figures. Thus, the small DRX grains promoted void nucleation.

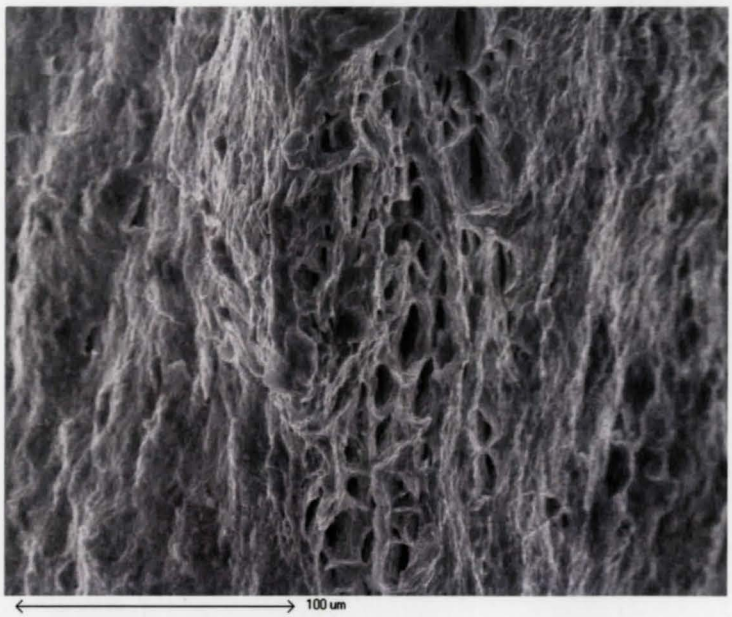

Figure 5.35 Fracture surface of R7 at 200°C $6.67\times10^{-4}s^{-1}$.The width direction is vertical.

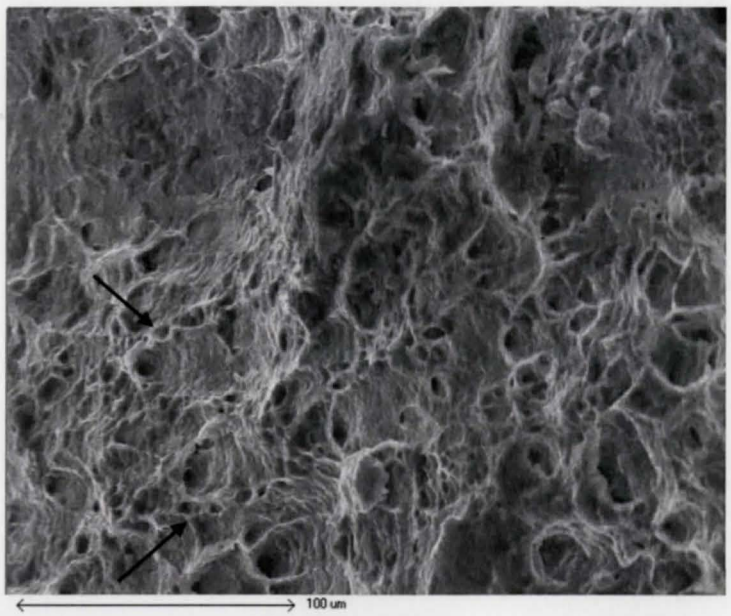

Figure 5.36 Fracture surface of E at 200°C $6.67\times10^{-4}s^{-1}$. The width direction is vertical.

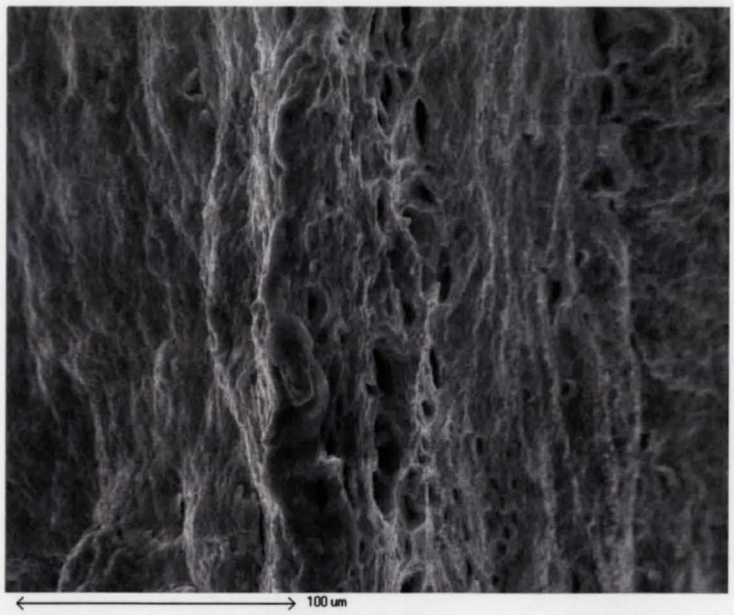

Figure 5.37 Fracture surface of R12 at 200°C $6.67\times10^{-4}s^{-1}$. The width direction is vertical.

Voids in R7 and R12 had an oval shape, while the voids in E were round. In an effort to explain this, the *r*-value (strain along the sample's width divided by the thickness strain) was measured at a point in the gauge length and at fracture. Table 5.3 shows the results. As each material necked, the thickness strain increased compared to the width strain. R7 and R12 had much lower *r*-values than E. This means that the stress normal to the sample's thickness was higher in R7 and R12. The voids became longer in the width direction, as this force compressed them.

Table 5.3 *r*-values at fracture for all three materials at 200°C $6.67\times10^{-4}s^{-1}$.

Material	Fracture	Gauge Section
R7	0.351	1.174
R12	0.435	1.331
E	1.387	1.859

6. Discussion

This chapter contains an analysis of the experimental data. Volume fractions of recrystallized grains and of grains oriented with a basal texture were analyzed. Flow properties were modeled with the constitutive equation for superplastic flow in magnesium alloys. The effects of grain size, texture, and recrystallization on formability are discussed.

6.1 Hall-Petch Relationship

The rolled material was annealed to a 12 μm grain size. This material was designated R12. Both these materials were tested in tension at 200°C $6.67\times10^{-4}s^{-1}$. R7 had a 0.2% yield strength of 78 MPa, while that of R12 was 66 MPa. A Hall-Petch plot was constructed to examine the grain size – yield strength relationship. Since only two grain sizes were tested, the data form a straight line with a friction stress (σ_0) of 27.03 MPa and a strength coefficient (k) of 134.83 MPa·$\mu m^{1/2}$. For room temperature tests, Wang et al. (2007) reported values of σ_0 and k to be 35.88 MPa and 142.53 MPa·$\mu m^{1/2}$. This was the low end of k values reported in the literature for AZ31 (see section 2.4.2). At 200°C, it is conceivable that σ_0 will be lower, since the higher temperature will increase the mobility of dislocations. The k value was low, but still reasonable. Since the Hall-Petch relationship was satisfied, it can be assumed that dislocation motion is the dominant deformation mode during the early stages of flow.

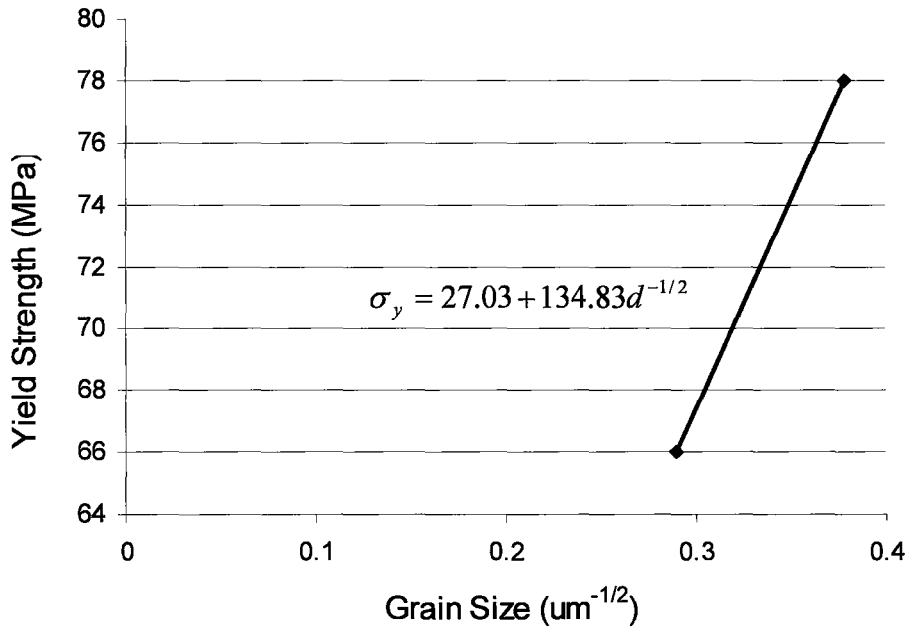

Figure 6.1 Hall-Petch relationship for R7 and R12.

6.2 Volume Fraction of Recrystallized Grains

Recrystallization occurred in all three materials at 200°C $6.67\times10^{-4}s^{-1}$. Figure 6.2 shows the relationship between fraction recrystallized (X_v) and strain. The data start at a strain of 0.15 because that was the strain at which X_v was measurable. At lower strains, only grain boundary serrations were visible. The figure ends at a strain of 0.30 because the onset of localized necking made a direct comparison of X_v at identical strains difficult. Table 6.1 gives the recrystallized fraction of each material at fracture. R7, with the smallest initial grain size, recrystallized at a faster rate than the 12 μm materials. A smaller grain size results in a greater grain boundary area, allowing for more nucleation sites. R7 recrystallized to completion, while the two 12 μm materials had some elongated grains present at fracture. R12 recrystallized to a greater extent than E. E also

recrystallized at a lower rate than R7 and R12. It is unclear why the DRX properties of E were so different than R12. In the two rolled materials, it was sometimes difficult to distinguish a recrystallized grain from an initial grain. Thus, any grain under 3 μm in size was considered to be recrystallized.

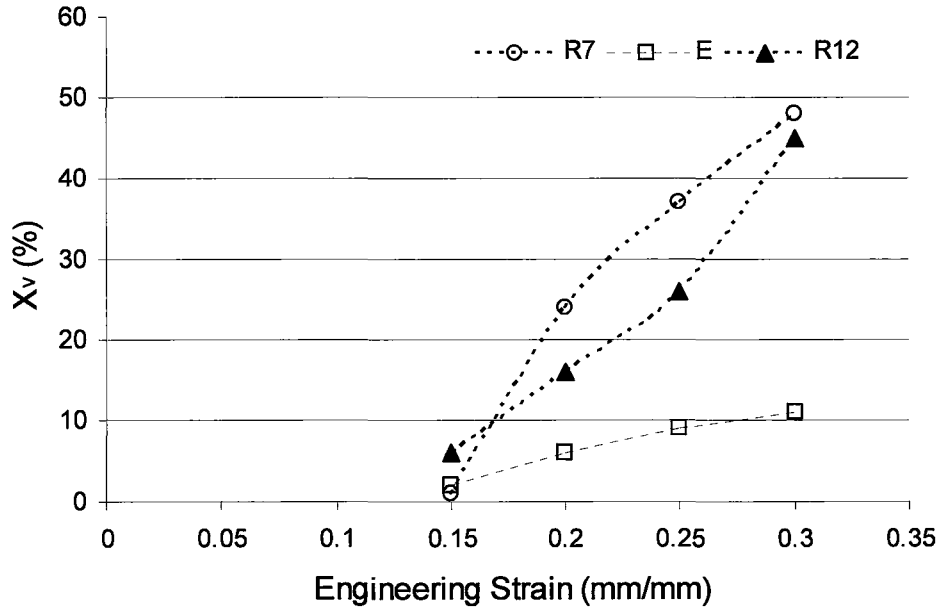

Figure 6.2 Recrystallized fraction versus engineering strain for R7, E, and R12 at 200°C $6.67\times10^{-4}s^{-1}$.

Table 6.1 Recrystallized fraction at failure R7, E, and R12 at 200°C $6.67\times10^{-4}s^{-1}$.

Material	X_v
R7	100
E	45
R12	85

6.3 Texture Analysis

The volume fraction (V_f) of grains with the basal plane oriented parallel to the rolling direction over several critical angles (β_c) was calculated from equation 4.5. Table 6.2 summarizes the results. A critical angle of 0° would mean that the normal to the basal plane and rolling direction are exactly perpendicular. As the critical angle increased, the volume fraction increased, since more grains had orientations with the *c*-axis near the sheet normal. E had V_f values that were higher than R7 and R12 at all critical angles. This agreed with the pole figures (Figures 5.3, 5.4, and 5.15). Annealing R7 to increase the grain size did little to the texture. This reinforced the conclusion that the difference in yield strength between these two materials was largely due to grain size effects. R12's softer texture could also have resulted in improved elongation over E. However, recrystallization in both materials would presumably have altered the texture, so no quantitative assessment can be made.

Table 6.2 Volume fraction of grains with a basal orientation for several critical angles.

Critical angle (°)	E	R7	R12
5	0.065	0.070	0.057
10	0.160	0.149	0.145
15	0.287	0.244	0.249
20	0.420	0.328	0.335

6.4 Constitutive Equation Modeling

Watanabe et al. (2001b) developed a constitutive equation for superplastic flow in magnesium alloys (see equations 2.1 and 2.2). An attempt was made to fit the data from

this project to equation 2.1, and compare this with the Hall-Petch data. This would help identify any transition in deformation mechanism. Table 6.3 displays the values used for each parameter in equations 2.1 and 2.2. The effective diffusion coefficient D_{eff} was calculated using equation 2.2 from equations 6.1 and 6.2:

$$\delta D_{gb} = 5.0 \times 10^{-12} e^{-\frac{Q_{gb}}{RT}} \tag{6.1}$$

$$D_L = 1.0 \times 10^{-4} e^{-\frac{Q_L}{RT}} \tag{6.2}$$

where R is the gas constant, T is the absolute temperature, Q_{gb} is the activation energy for grain boundary diffusion, and Q_L is the activation energy for lattice diffusion in magnesium (Somekawa et al. (2005)). D_{eff} was calculated to be 2.76×10^{-18} m^2/s for R7, 1.66×10^{-18} m^2/s for R12, and 9.36×10^{-18} m^2/s for a recrystallized material with a 2 μm grain size. Grain boundary sliding was assumed to be the operative deformation mechanism for the constitutive modeling. Thus, an n value of 2 was used.

Table 6.3 Data used in constitutive modeling at 200°C $6.67\times10^{-4}s^{-1}$.

Parameter	Value	Source
Q_{gb}	92 000 J/mol	Somekawa et al. (2005)
Q_L	135 000 J/mol	Somekawa et al. (2005)
R	8.314 J/K mol	
D_L	1.233×10^{-19} m^2/s	this work
δD_{gb}	3.457×10^{-22} m^3/s	this work
x	1.7×10^{-2}	Watanabe et al. (2004)
D_{eff}	2.76×10^{-18} m^2/s, 1.66×10^{-18} m^2/s, 9.36×10^{-18} m^2/s	this work
G	17 GPa	Housh et al. (1990)
k	1.38×10^{-23} $m^2 kg\ s^{-2}K^{-1}$	
b	3.21×10^{-10} m	Somekawa et al. (2005)
$\dot{\varepsilon}$	6.67×10^{-4} s^{-1}	this work
d	2 μm, 7 μm, 12 μm	this work

Figure 6.3 plots applied stress versus $d^{1/2}$ for the constitutive equation (2.1) and the Hall-Petch equation. The initial grain sizes of 7 and 12 μm, as well as the recrystallized grain size of 2 μm are indicated in the figure. Initially, dislocation slip was the dominant deformation mechanism. The presence of strain hardening and the satisfaction of the Hall-Petch relationship are evidence of dislocation activity. According to the constitutive equation, the required stress for GBS at these grain sizes was much higher (149 and 328 MPa) than the stresses measured during tensile testing at 200°C. At a grain size of 5 μm, the stress necessary for GBS drops below the stress produced from grain boundary - dislocation interactions. As DRX took place, the grain size was reduced to 2 μm, where the stress required for GBS was only 23 MPa, according to equation 2.1. Thus, as the materials recrystallized, GBS became the dominant deformation mechanism. This explained the softening observed in the flow curves shown in Figure 5.17. As DRX occurred, the stress required to deform the material dropped, since GBS became the dominant deformation mechanism. DRX in E occurred at a slower rate and to a lesser extent than in the rolled materials (see Figure 6.2). This explained the short plateau stress observed in E, as well as the lesser amount of softening in E (Figure 5.17). The slower rate of DRX delayed the onset of material softening, as slip would remain operative at larger strains.

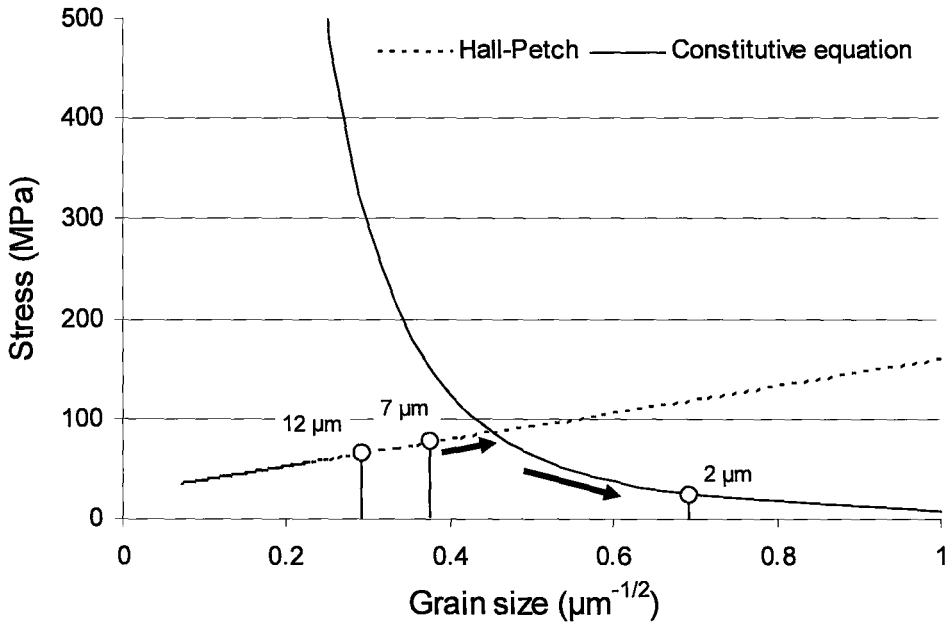

Figure 6.3 Stress versus $d^{1/2}$ showing the transition from slip to GBS at 200°C $6.67\times10^{-4}s^{-1}$.

R7 and R12 had elongations of 66.9 and 65.6%, while that of E was only 51.2%. The increased amount of grain boundary sliding in the rolled materials could explain this. After the transition from slip to GBS, the materials became almost superplastic. Since the rate and extent of DRX was higher in the rolled materials, this pseudo-superplastic regime would start at lower strains and be more stable than in the extruded material. A longer period of GBS would results in greater elongations. This would also explain why R7 and R12 had similar elongations. Both materials recrystallized to the same grain size, allowing GBS to control the flow behaviour to fracture.

A transition to GBS with a 2 μm grain size could also explain the void formation in E. Microcracking has been shown to form at the fine/coarse grain interface (Bussiba et

al. (2001)). With GBS dominant at small grains and slip dominant in the larger grains, voids will be likely to form in E at these interfaces.

6.5 Rolled Versus Extruded Magnesium Sheet

The chemistry of the rolled and extruded materials was quite similar (Table 4.1). The grain size effect was eliminated by annealing the rolled material to a 12 μm grain size. Texture measurements indicated that both materials possessed a basal texture of similar intensity (Table 6.2). The sole difference was the amount of DRX grains as deformation proceeded (Figure 6.2 and Table 6.1). GBS also became the dominant deformation mechanism as more DRX grains were generated. The rolled material softened to a greater degree because of this, because the stress necessary for GBS was much less than that produced by slip. Since there were more DRX grains in R12 than in E, GBS was more prevalent, and its elongation was larger as a result.

7. Conclusions

The conclusions reached in the present work are stated below:

1. DIC has been used to measure local strain causing tensile instability at room temperature and at 200°C. These local strains are within 5% of those predicted through the instability condition.
2. The rolled material obeyed the Hall-Petch relationship during the initial stages of deformation at 200°C $6.67\times10^{-4}s^{-1}$. The k value was 134.83 $MPa\cdot\mu m^{1/2}$.
3. DRX occurred in all three materials. New grains of approximately 2 μm in size nucleated at the grain boundaries. R7 recrystallized completely, while E and R12 had larger, elongated grains present at fracture. At fracture, 85% of R12 recrystallized, while only 45% of E had recrystallized. E recrystallized at a lower rate than the rolled materials.
4. A transition in deformation mechanism from slip to GBS occurs as the grain size is decreased. At the initial grain sizes of 7 and 12 μm, the stress required for GBS was 149 and 328 MPa. As the grain size was reduced, the stress required for GBS decreased to 23 MPa, resulting in softening in R7 and R12.
5. Comparing R12 and E, the grain size, texture, and chemistry differences were only slight. Therefore, the extent of recrystallization caused the difference in elongation. Using fine grained alloys, or alloys processed under conditions where DRX can take place, will improve formability in magnesium sheet materials.

Bibliography

Al-Samman, T., & Gottstein, G. 2008. Materials Science & Engineering A, 490, 411-420.

Aramis – deformation measurement using the grating method, Users Manual, v 4.7.4-2, 2001. GOM mbH.

Backx, P., & Kestens, L. 2005. Materials Science Forum, 495-497, 633-638.

Bang, W., Sung, H.J., Kim, I.J., Choo, D., Park, W.J., Jung, I.H., & Ahn, S. 2006. *Magnesium Technology 2006*. 249-252.

Barnett, M.R. 2003a. Metallurgical and Materials Transactions A, 34A, 1799-1806.

Barnett, M.R. 2003b. Materials Transactions, 44(4), 571-577.

Barnett, M.R. 2007. *Magnesium Technology 2007*. 29-32.

Barnet, M.R., Atwell, D., & Beer, A.G. 2004a. Materials Science Forum, 467-470, 435-440.

Barnett, M.R., Keshavarz, Z., Beer, A.G., & Atwell, D. 2004b. Acta Materiala, 52, 5093-5103.

Bhattacharya, B. 2006. *Plastic Deformation Behaviour of Pure Magnesium in the Temperature Range 4.2K-300K*. Ph.D thesis, McMaster University.

Bohlen, J., Nurnberg, M.R., Senn, J.W., Letzig, D., Agnew, S.R. 2007. Acta Materiala, 55, 2101-2112.

Bussiba, A., Ben Srtzy, A., Schtechman, A., Ifergan, S., & Kupiec, M. 2001. Materials Science & Engineering A, 302, 56-62.

Callister, W.D. 2003. *Materials Science and Engineering: An Introduction 6th ed.* John

Wiley & Sons.

Chapman, J.A., & Wilson, D.V. 1962-3. Journal of the Institute of Metals, 91, 39-40.

del Valle, J.A., Carreno, F., & Ruano, O.A. 2006. Acta Materiala, 54, 4247-4259.

Dieter, G.E. 1986. *Mechanical Metallurgy, 3rd ed.* McGraw-Hill.

Emley, E.F. 1966. *Principles of Magnesium Technology*. Pergamon Press.

Gehrmann, R., Frommert, M.R., & Gottstein, G. 2005. Materials Science & Engineering A, 395, 338-349.

Gifkins, R.C. & Langdon, T.G. 1965. Journal of the Institute of Metals, 93, 347-352.

Godara, A., & Raabe, D. 2007. Composites Science & Technology, 67, 2417-2427.

Hall, E.O. 1951. Proceeds of the Physical Society, 64B, 747-753.

Hauser, F.E., Starr, C.D., Tietz, L., & Dorn, J.E. 1955. Transactions of the ASM, 47, 102-131.

Hauser, F.E., Landon, P.R., & Dorn, J.E. 1956. Transactions of the ASM, 48, 986-1002.

Housh, S., Mikuchi, B., & Stevenson, A. 1990. *ASM Handbook Vol. 2*. ASM International.

Huang, G., Wang, L., Huang, G., & Pan, F. 2005. Materials Science Forum, 488-489, 215-218.

Huang, Z.W., Yoshida, Y., Kamado, S., Kojima, Y. 2005. Materials Science Forum, 488-489, 593-596.

Hwang, S., Nishimura, C., & McCormick, P.G. 2001. Scripta Materiala, 44, 1507-1511.

Ion, S.E., Humphreys, F.J., White, S.H. 1982. Acta Metallurgica, 30, 1909-1919.

Ishihara, S., Nan, Z., & Goshima, T. 2007. Materials Science & Engineering A, 468-470,

214-222.

Itoh, G., Motohashi, Y., & Iseno, Y. 2004. Materials Science Forum, 447-448, 395-402.

Jager, A., Lukac, B., Gartnerova, V., Bohlen, J., & Kainer, K.U. 2004. Journal of Alloys and Compounds, 378, 184-187.

Jager, A., Lukac, B., Gartnerova, V., Haloda, J., & Dopita, M. 2006. Materials Science & Engineering A, 432, 20-25.

Jain, A., & Agnew, S.R. 2007. Materials Science & Engineering A, 462, 29-36.

Jin, H., & Lloyd, D.J. 2004. Scripta Materiala, 50, 1319-1323.

Jin, H.K., Huang, J.C., & Langdon, T.G. 2005. Materials Science & Engineering A, 402, 250-257.

Kang, J., Jain, M., Wilkinson, D.S., & Embury, J.D. 2005. Journal of Strain Analysis, 40(6), 559-570.

Kang, J., Ososkov, Y., Embury, J.D., & Wilkinson, D.S. 2007. Scripta Materiala, 56, 999-1002.

Kelley, W., & Hosford, W.F. Jr. 1968. Transactions of the Metallurgical Society of AIME, 242, 654-661.

Kim, S.H., You, B.S., Yim, C.D., Seo, Y.M. 2005. Materials Letters, 59, 3876-3880.

Kim, W.J., Hong, S.I., Kim, Y.S., Min, S.H., Jeong, H.T., & Lee, J.D. 2003. Acta Materiala, 51, 3292-3307.

Kim, W.J., Lee, J.B., Kim, W.Y., Jeong, H.T., & Jeong, H.G. 2007. Scripta Materiala, 56, 309-312.

Lahaie, D., Embury, J.D., Chadwick, M.M., & Gray, G.T. 1992. Scripta Metallurgica et

Materiala, 27(2), 139-142.

Langdon, T.G. 1994a. Materials Science & Engineering A, 174, 225-230.

Langdon, T.G. 1994b. Materials Science Forum, 170-172, 53-58.

Li, L., Lijia, C., & Zheng, L. 2005. Materials Science Forum, 488-489, 585-588.

Lim, H.T., Kang, J.H., Han, J.W., Hwang, S.K., & Kim, Y.W. 2006. Materials Science Forum, 510-511, 498-501.

Luo, A.A., & Sachdev, A.K. 2007. Metallurgical & Materials Transactions A, 38, 1184-1192.

Lyons, J.S., Liu, J. & Sutton, M.A. 1996. Experimental Mechanics, 36(1), 64-70.

Mabuchi, M., Shimojima, K., Yamada, Y., Wen, C.E., Nakamura, M., Asahina, T., Iwasaki, H., Aizawa, T., & Higashi, K. 2001. Materials Science Forum, 357-359, 327-332.

Mabuchi, M., Chino, Y., Iwasaki, H., Aizawa, T., & Higashi, K. 2001. Materials Transactions, 42(7), 1182-1189.

Mabuchi, M., Ameyama, K., Iwasaki, H., & Higashi, K. 1999. Acta Materiala, 47(7), 2047-2057.

Mackenzie, L.W.F., Lorimer, G.W., Humphreys, F.J., & Wilks, T. 2004. Materials Science Forum, 467-470, 477-482.

Marya, M., Hector, L.G., Verma, R., & Tong, W. 2006. Materials Science & Engineering A, 418, 341-356.

Meyers, M.A., Vohringer, O., & Lubarda, V.A. 2001, Acta Materiala, 49, 4025-4039.

Miyahara, Y., Horita, Z., & Langdon, T.G. 2006. Materials Science & Engineering A,

420, 240-244.

Mohri, T., Mabuchi, M., Nakamura, M., Asahina, T., Iwasaki, H., Aizawa, T., & Higashi, K. 2000. Materials Science & Engineering A, 290, 139-144.

Mukai, T., Yamanoi, M., Watanabe, H., Ishikawa, K., & Higashi, K. 2001a. Materials Transactions, 42(7), 1177-1181.

Mukai, T., Yamanoi, M., Watanabe, H., Ishikawa, K., & Higashi, K. 2001b. Scripta Materiala, 45, 89-94.

Mukherjee, A.K., Bird, J.E., & Dorn, J.E. 1969. Transactions of the ASM, 62, 155-179.

Murty, K L, 2003, Materials Science Forum, 426-423, 3575-3580.

Nieh, T.G., Wadsworth, J., & Sherby, O.D. 1997. *Superplasticity in Metals and Ceramics*. Cambridge University Press.

Ono, N., Nowak, R., Miura, S. 2003. Materials Letters, 58, 39-43.

Ono, N., Ueda, M., Miura, S. 2005. Materials Science Forum, 488-489, 555-558.

Ohyama, R., Koike, J., Kobayashi, T., Suzuki, M., & Maruyama, K. 2003. Materials Science Forum, 419-422, 237-242.

Partridge, P.G. 1967. Metallurgical Reviews, 12, 169-194.

Petch, N.J. 1953. Journal of the Iron and Steel Institute, 174, 25-28.

Perez-Prado, M.T., & Ruano, O.A. 2002. Scripta Materiala, 46, 149-155.

Perez-Prado, M.T., del Valle, J.A., & Ruano, O.A. 2004. Materials Science Forum, 447-448, 221-226.

Ponge, D., & Gottstein, G. 1998. Acta Materiala, 46(1), 69-80.

Reed-Hill, R.E., & Robertson, W.D. 1957. Acta Metallurgica, 5, 717-727.

Sherby, O.D., Caligiuri, R.D., Kayali, E.S., & White, R.A. 1981. *Advances in Metal Processing*. Plenum Press.

Sitdikov, O., Kaibyshev, R., & Sakai, T. 2003. Materials Science Forum, 419-422, 521-526.

Somekawa, H., Hirai, K., Watanabe, H., Takigawa, Y., & Higashi, K. 2005. Materials Science and Engineering A. 407, 53-61.

Song, J-W., Kim, C-W., Han, J-W., Kim, M-S., & Hwang, S-K. 2003. Materials Science Forum, 439, 227-232.

Srivastava, V., McNee, K.R., Greenwood, G.W., & Jones, H. 2004. Materials Science and Technology, 20, 42-46.

Stanford, N., & Barnett, M.R. 2008. Materials Science & Engineering A, 496, 399-408.

Styczynski, A, Hartig, Ch., Bohlen, J., & Letzig, D. 2004. Scripta Materiala, 50, 943-947.

Tan, J.C., & Tan, M.J. 2003. Materials Science & Engineering A, 339, 124-132.

Vahsentsev, Yu.G., & Isaev, V.V. 1988. Strength of Materials, 20(4), 495-499.

Vespa, G., Mackenzie, L.W.F., Verma, R., Zarandi, F., Essadiqi, E., & Yue, S. 2008. Materials Science & Engineering A, 487, 243-250.

Wang, J.K., Yin, D.L., Zhu, X.R., Wang, R., & Zhao, X. 2007.*Magnesium Technology 2007*, 169-176.

Wang, K.L., Yu, Y., & Wang, E.D. 2005. Materials Science Forum, 488-489, 535-538.

Wang, Y., Zeng, X., Ding, W., Luo, A.A., & Sachdev, A.K. 2007. Metallurgical and Materials Transactions A, 38A, 1358-1366.

Watanabe, H., Mukai, T., Higashi, K. 2004. Materials Science Forum, 447-448, 91-96.

Watanabe, H., Mukai, T., Ishikawa, K. 2007. Journal of Materials Processing Technology 182, 644-647.

Watanabe, H., Mukai, T., Ishikawa, K., Mohri, T., Mabuchi, M., & Higashi, K. 2001a. Materials Transactions, 42(1), 157-162.

Watanabe, H., Mukai, T., Ishikawa, K., Mabuchi, M., & Higashi, K. 2001c. Materials Science & Engineering A, 307, 119-128.

Watanabe, H., Mukai, T., Ishikawa, K., & Higashi, K. 2002. Scripta Materiala, 46, 851-856.

Watanabe, H., Mukai, T., Mabuchi, M., & Higashi, K. 1999a. Scripta Materiala, 41(2), 209-213.

Watanabe, H., Mukai, T., Mabuchi, M., & Higashi, K. 2001b. Acta Materiala, 49, 2027-2037.

Watanabe, H., Mukai, T., Kohzu, M., Tanabe, S., & Higashi, K. 1999b. Acta Materiala, 47(14), 3753-3758.

Watanabe, H., Tsutsui, H., Mukai, T., Ishikawa, K., Okanda, Y., Kohzu, M., & Higashi, K. 2000. Materials Science Forum, 350-351, 171-176.

Wei, Y.H., Wang, Q.D., Zhu, Y.P, Zhou, H.T., Ding, W.J., Chino, Y., & Mabuchi, M. 2003. Materials Science & Engineering A, 360, 107-115.

Wilson, D.V. 1970. Journal of the Institute of Metals, 98, 133-143.

Xue, F., Du, W., & Sun, Y. 2005. Materials Science Forum, 488-489, 143-146.

Yang, X., Miura, H., & Sakai, T. 2005. Materials Transactions, 46(12), 2981-2987.

Yi, S.-B., Davies, C.H.J., Brokmeier, H.-G., Bolmaro, R.E., Kainer, K.U., & Homeyer, J.

2006. Acta Materiala, 54, 549-562.

Yoshinaga, H. & Horiuchi, R. 1963. Transactions of the Japan Institute of Metals, 5, 14-21.